Research article

The stable isotope fractionation of neodymium on ferrihydrite revisited

Mark Nestmeyer[1,2]✉ Alex J. McCoy-West[1,3] Yuan Mei[2] Kevin W. Burton[4]

[1] IsoTropics Geochemistry Laboratory, Earth and Environmental Science, James Cook University, Townsville, QLD 4811, Australia
[2] CSIRO Mineral Resources, Kensington, WA 6151, Australia
[3] Economic Geology Research Centre, James Cook University, Townsville, QLD 4811, Australia
[4] Department of Earth Sciences, Durham University, Elvet Hill, Durham DH1 3LE, UK

✉ **Correspondence to:** Mark Nestmeyer: mark.nestmeyer@my.jcu.edu.au

Author contributions: Conceptualization: MN, AJMC-W; Data curation: MN; Formal analysis: MN, AJMC-W; Funding acquisition: AJMC-W, YM; Investigation: MN, AJMC-W; Methodology: MN, AJMC-W, YM, KWB; Project administration: AJMC-W; Resources: AJMC-W, YM, KWB; Software: MN, YM; Supervision: AJMC-W, YM; Validation: MN, AJMC-W, YM, KWB; Writing – original draft: MN; Writing – review & editing: AJMC-W, YM, KWB

Data, code, and outputs: Nestmeyer et al. (2026) https://doi.org/10.25903/tfqa-tt39

Submitted: 2025-12-30
Accepted: 2026-04-02
Published: 2026-06-18

Production editor:
Ryan Ickert

Handling editor:
Claire Rollion-Bard,
Daniel Ibarra

Reviews:
Jianghao Bai
and one anonymous reviewer

Copyediting:
Anselm Loges,
Marthe Klöcking

Ferrihydrite is a ubiquitous scavenger in aqueous environments that removes large amounts of dissolved metals thus it is pivotal to global geochemical cycles. Previous work found contradictory directions of stable isotope fractionation amongst light rare earth elements (REE) between aqueous solutions and ferrihydrite. Here, the isotope fractionation of $^{146}Nd/^{144}Nd$ on ferrihydrite has been revisited using a double spike that corrects for mass fractionation during sample processing. Surprisingly, contrary to previous observations, Nd on ferrihydrite was found to be enriched in lighter isotopes compared to Nd in aqueous solution by $10^3 \ln \alpha_{Sol\text{-}Liq} = -0.113 \pm 0.030$. We also report the first data set of stable $\delta^{146/144}Nd$ isotopes in seawater samples which are isotopically heavier than Fe-Mn (hydr)oxides by 0.357 ‰ on average. This is consistent with the scavenging of lighter Nd isotopes by ferrihydrite seen in the adsorption experiments. The fractionation is, however, much larger than observed in the experiments. This can be explained by carbonate complexes being the predominant aqueous complex of Nd in seawater which are isotopically heavier than free Nd by 0.107 ‰. However, additional data on natural samples is required to elucidate heterogeneities in seawater and Fe-Mn oxides in marine sediments. The enrichment of lighter Nd in the surface complex can be best explained by stiffer bonds in the aqueous complex which is demonstrated by a lower Debye-Waller factor (σ^2). This study lays the foundation for understanding the geochemical cycling of Nd and other REE between Earth's crust and hydrosphere using stable isotope signatures.

1 Introduction

Recent advances in analysing stable isotope ratios of rare earth elements (REE) have allowed their application to understanding their geochemical cycles between Earth's major reservoirs (Bai et al., 2025, 2024; McCoy-West et al., 2021, 2017, 2020a; Yu et al., 2025). Previous studies have found limited stable isotope fractionation in igneous systems for Ce and Nd (Bai et al., 2022; Liu et al., 2025b; McCoy-West et al., 2021, 2020a, 2022; Nestmeyer and McCoy-West, 2026; Pourkhorsandi et al., 2021) most likely due to the high temperature in those systems (> 800 °C) which reduces the magnitude of equilibrium isotope fractionation. Whereas studies concerned with low temperature systems like weathering profiles and seafloor sediments have observed larger isotope fractionation (Bai et al., 2025, 2023; Kaufmann and McCoy-West, 2025; Liu et al., 2023). For example, mid-ocean ridge basalts show a $^{146}Nd/^{144}Nd$ composition of −0.061 to −0.013 ‰ ($\Delta = 0.048$ ‰; McCoy-West et al., 2021). By contrast, Bai et al. (2025) found a variability of $^{146}Nd/^{144}Nd$ in different phases in a marine sediment core from −0.147 to 0.114 ‰ ($\Delta = 0.261$ ‰) and Bai et al. (2023) found a range of −0.152 to 0.058 ‰ ($\Delta = 0.210$ ‰) within a single basaltic soil weathering profile.

High precision analysis of stable REE isotopes is still in its infancy and isotopic data of a wider spectrum of sample types including natural waters and sediments is warranted to understand the interplay of sinks and sources in the geochemical cycle of REE. Following a previous study on isotope fractionation of light REE between aqueous complexes (Nestmeyer and McCoy-West, 2025), here we

extend the isotope fractionation of REE in aqueous systems to their interaction with minerals, notably ferrihydrite.

Ferrihydrite is a hydrous Fe oxide that forms nanoparticles and is ubiquitous in the environment. It is a so-called 'scavenger', is other words, it adsorbs large amounts of metal cations (Ni^{2+}, Cu^{2+}, Zn^{2+}, REE^{3+}) and oxyanions (PO_4^{3-}, CrO_4^{2-}, AsO_4^{3-}) from the surrounding water column due to its large surface to volume ratio (Hiemstra et al., 2010; Waychunas et al., 2005). Ferrihydrite is also the precursor of other common Fe oxides such as lepidocrocite, goethite, and hematite which occur in soils and are the constituents of iron sediments and ferromanganese crusts and nodules that cover large parts of the modern ocean and host large amounts of REE. Ferrihydrite also occurs in acid mine tailings and is used for water purification and detoxification because of its capability to adsorb vast amounts of pollutants (Cornell and Schwertmann, 2003; Spadini et al., 2003). In addition to adsorption, incorporation of metals into the crystal lattice of ferrihydrite scavenges metals from the water column. This mechanism is not explored here since the surface capacity of mineral suspensions is much larger than the capacity of their crystal lattices.

Previous studies investigated the surface complexation of light REE (La, Ce, Pr, Nd) on ferrihydrite and birnessite (δ-MnO_2) and the associated isotope fractionation between aqueous and surface complexes using adsorption experiments and extended X-ray absorption fine structure (EXAFS) (Nakada et al., 2013a, 2017, 2013b). Noticeably, it was found that adsorption of Ce on ferrihydrite induces an enrichment of lighter isotopes in the surface complex and leaves the aqueous solution enriched in heavy isotopes. In marked contrast, Nd and Sm were found to be isotopically heavier on ferrihydrite compared to their species in aqueous solution. Analysis with EXAFS demonstrated that the light REE (La, Ce, Pr, and Nd) all had similar REE-O bond lengths but a lower number of neighbour oxygen atoms on ferrihydrite compared to their aqueous complexes (Nakada et al., 2013b). A similar change in atomic coordination during the adsorption onto ferrihydrite is, therefore, at odds with the observed contradictory isotope fractionation. Cerium, unlike other light REE, can oxidize to a tetravalent state which could potentially explain an opposing isotope fractionation. However, ferrihydrite evidently does not oxidise Ce (Nakada et al., 2013a) and the reason for such a discrepancy must lie somewhere else. Nakada et al. (2013b) used an equilibration time of 6 h, but they did not monitor kinetic effects in time series experiments. Furthermore, they only reported time series data for the liquid phase of Ce experiments which does not provide information on the change in isotopic composition between solid and liquid phase through time which would be required to unequivocally assess the isotopic equilibration time. The previously published data of the atomic coordination of light REE on ferrihydrite, therefore, might not represent their equilibrium coordination environment.

In this study a range of adsorption experiments including time series experiments were performed to understand the equilibration time and isotope fractionation for the adsorption of Nd onto ferrihydrite. Isotope analyses were performed using the double spike method which corrects for isotope fractionation occurring during mass spectrometry and sample processing meaning the yields from ion-exchange chromatography are not crucial. In addition, ab initio molecular dynamics simulations were performed to model the atomic coordination of Nd in aqueous solution and on a ferrihydrite surface to understand the isotope fractionation from a quantum chemical perspective. We also present the first dataset of stable Nd isotope composition of seawater samples to improve our understanding of the underexplored geochemical cycle of REE. This study lays the groundwork for identifying the major sinks and sources of REE in the World's oceans and rivers and potentially finds application in industrial applications like acid mine drainage.

2 Methodology

2.1 Adsorption experiments

Adsorption experiments were performed in a fume cupboard in the IsoTropics Geochemistry Laboratory, James Cook University. All acids used were double distilled using Savillex® DST-1000 distillation units and all labware was acid-leached with 2 mol/L HNO_3 for at least three weeks.

A batch of 2-line-ferrihydrite was synthesised following the procedure described in Cornell and Schwertmann (2003). A 1 mol/L KOH solution (99.99 %; Sigma-Aldrich®) was added dropwise to a 0.1 mol/L $FeN_3O_9 \cdot 9H_2O$ ($\geq$ 99.999 %; Sigma-Aldrich®) solution in a 125 mL Nalgene® FEP bottle under stirring until the pH reached 7-8. The pH was monitored and stabilised above 7 for another 15 minutes. The yielded suspension was centrifuged for 10 minutes, and the liquid was subsequently removed. The paste was then washed three times with fresh MilliQ® ultrapure water using centrifugation. An aliquot of the mineral paste was removed and air dried by constant air flow in a fume cupboard overnight. The dried material was identified using X-ray diffraction performed on a Siemens D5000 X-ray diffractometer equipped with a graphite monochromator and CuKα radiation. A diffraction angle from 10° to 80° 2ϑ was used with a step size of 0.02° 2ϑ and an acquisition time of 10 s per step.

A Nd stock solution was prepared by diluting a 1000 µg/mL Nd high purity standard (HPS; Lot# = 2122829-100) in MilliQ® ultrapure water to a concentration of 20 µg/mL. The synthesised ferrihydrite paste was diluted in 500 mL MilliQ® ultrapure water and vigorously stirred for 90 min on a magnetic stirrer to create a stock suspension. Individual adsorption experiments were conducted on a Ratek® gyratory mixer in loosely capped 125 mL Nalgene® FEP bottles to let the experiments equilibrate with the atmosphere. Each experiment contained an aliquot of the ferrihydrite stock suspension and a NaCl ($\geq$ 99.5 %; Sigma-Aldrich®) background solution. The suspension was equilibrated with the background electrolytes for 20 h before 3 mL of the Nd stock (60 µg Nd) were added dropwise, over a period of 1-2 minutes to avoid local oversaturation, which

marked the start of the reaction. The final experiment had a NaCl concentration of 0.01 mol/L and a volume of 50 mL. The pH of the experiments was adjusted to 5.5 by adding 0.1 mol/L and 0.01 mol/L KOH. The adsorption edge of Nd on ferrihydrite is between pH = 5.0 and 6.0 (Bau, 1999) but varies with the amount of ferrihydrite in the experiment. A pH of 5.5 is lower than natural waters but was required to avoid complete adsorption of Nd. In order to constrain the time required for the system to achieve isotopic equilibrium, a time series experiment was conducted which contained identical experiments (i.e. input solutions) that ran for variable durations (0.5-168 h). Following the time series experiments, another set of experiments containing variable amounts of ferrihydrite were undertaken that lasted for at least 48 h (see Section 3 Results) to constrain the isotope fractionation factor. For experiments that ran longer than 24 h, the pH was adjusted daily back to 5.5. After the reaction time, experiments were centrifuged for 10 minutes. The liquid was separated by pipetting and subsequently filtering through a 0.22 µm PTFE filter membrane. The remaining ferrihydrite paste was then digested in 6 mol/L HCl. The solid and liquid phases were evaporated to dryness in Savillex® PFA vials on a hotplate and then diluted in 5 mL or 10 mL of 2 mol/L HNO_3, respectively. An aliquot of 0.1 mL was volumetrically acidified with 4.9 mL of 2 % HNO_3 for trace element analysis using a Thermo Fisher Scientific® iCAP TQ-ICP-MS. The analyses were performed using a 3-point calibration of Nd-Fe solutions presented in Supplementary Table S1 (see Supplementary Material).

Modelling of the aqueous speciation of Nd in the experiments and a simplified seawater was done in PHREEQC (Parkhurst and Appelo, 2013) using the Lawrence Livermore National Laboratory (LLNL) database. The simulated solution reflects the experimental parameters of pH = 5.5, Nd = 60 µg, and NaCl = 0.01 mol/L. For the simplified seawater, concentrations of anions were taken from Diehl and Bach (2020) and are presented in Table S2.

2.2 Seawater sampling

Seawater samples were collected from Seaham pier (northern England) in August 2017. Five water samples were collected from the same site in pre-cleaned 10 L containers. Alkalinity was determined by titration. Within 8 h, the water was filtered through 0.2 µm cellulose-acetate filters using a pressurised Teflon unit. Sample locations and field measurements, including pH, temperature, alkalinity, and total dissolved solids (TDS), are given in Nestmeyer et al. (2026).

2.3 Isotopic analysis

2.3.1 Isotopic analysis of adsorption experiments

Isotope measurements of the adsorption experiments were undertaken in the IsoTropics Geochemistry Laboratory, JCU. Following trace element analysis, samples were completely evaporated and diluted in 5 mL of 6 mol/L HCl. Aliquots containing 100 ng Nd were separated and spiked using a ^{145}Nd-^{150}Nd double spike (McCoy-West et al., 2020b) and refluxed in 2 mL of 16 M HNO_3 at 120 °C for at least 4 h for spike-sample equilibration. Samples were again evaporated to dryness and diluted in 2 mL of 1 mol/L HCl for ion exchange chromatography. Neodymium was isolated following a slightly modified protocol from McCoy-West et al. (2020b). The protocol contains a first separation of REE from the bulk matrix and a subsequent separation of Nd from other REE to account for small impurities in the Nd dopant. First, BioRad® columns were filled with 2 mL AG50W-X8 cation exchange resin. The resin was cleaned with 1 column load of 6 M HCl and conditioned with 5 mL of 1 mol/L HCl. The bulk matrix was eluted in 10 mL of 1 M HCl plus HF, 12 mL of 2.5 mol/L HCl and 10 mL of 2 mol/L HNO_3. The REE fraction was collected in 13 mL of 6 mol/L HCl.

The collected REE fraction was evaporated and diluted in 0.5 mL of 0.2 mol/L HCl. Neodymium was separated from REE using polypropylene columns filled with Eichrom® lanthanide specific resin. The resin was cleaned with 1 column load of single-distilled 6 mol/L HCl and 1 column load of single-distilled 1 mol/L HCl. The sample was loaded after conditioning with 0.5 mL of 0.2 mol/L HCl. The matrix was eluted in 5 mL of 0.2 mol/L HCl, and Nd was collected in 6 mL of 0.2 mol/L HCl and evaporated to dryness. Three drops of 16 mol/L HNO_3 were added to remove any organic residues. Samples were finally diluted in 0.5 mL of 0.5 mol/L HNO_3 for isotopic analysis by multi-collection plasma source mass spectrometry (MC-ICP-MS) using a Thermo Fisher Scientific® Neptune.

Measurements were performed in dry plasma mode using a Cetac Aridus III desolvator. Each sample was analyzed for 100 cycles of data acquisition (4 s integrations), with 90 s washout between samples. The cup configuration used was L4 = ^{142}Nd, L3 = ^{143}Nd, L2 = ^{144}Nd, L1 = ^{145}Nd, C = ^{146}Nd, H1 = ^{147}Sm, H2 = ^{148}Nd, H3 = ^{149}Sm, and H4 = ^{150}Nd. The double spike deconvolution was carried out on the raw signals after Dodson (1963) using an in-house Mathematica code and is described in McCoy-West et al. (2020b) and was subsequently modified by Kaufmann and McCoy-West (2025). The double spike deconvolution yields values for stable ^{146}Nd/^{144}Nd ratios and calculates propagated uncertainties using the 95 % standard error from a Monte Carlo simulation. The measured isotope ratios were then normalized by the JNdi-1 standard, measured every two unknowns, by linear interpolation of the bracketing standard measurements. Isotope ratios are finally reported as deviation from the JNdi-1 standard in per mille:

$$\delta^{146}Nd = \left[\frac{(^{146}Nd/^{144}N)_{sample}}{(^{146}Nd/^{144}N)_{JNdi-1}} - 1\right] \times 10^3 \quad (1)$$

The difference in isotopic composition between the solid and liquid phase is reported as Δ-notation:

$$\Delta^{146}Nd_{Sol-Liq} = \delta^{146}Nd_{Sol} - \delta^{146}Nd_{Liq} \quad (2)$$

Two laboratory standards "Merck" and "MONA" (1000 µg/g Nd) were used as secondary standards during the analysis sessions yielding average δ^{146}Nd values of -0.086 ± 0.015 ‰

Table 1. Overview of adsorption experiments.

Expt.	Duration (h)	Fhy stock (mL)	Nd sorbed (%)	$\delta^{146}Nd_{Liquid}$ (‰)	2×SD (‰)	n	$\delta^{146}Nd_{Solid}$ (‰)	2×SD (‰)	n	$\Delta^{146}Nd_{Solid\text{-}Liquid}$ (‰)	Prop. uncert. (‰)	Mass balance (‰)
Time series												
1	0.5	1.00	5.44	0.020	0.010	3	−0.172	0.018	3	−0.193	0.021	0.013
2	1	1.00	8.12	−0.003	0.016	3	−0.141	0.032	3	−0.137	0.036	−0.010
3	3	1.00	8.21	−0.005	0.026	2	−0.121	0.024	3	−0.116	0.036	−0.011
4	6	1.00	8.22	0.003	0.007	3	−0.123	0.017	3	−0.126	0.019	−0.003
5	12	1.00	8.69	0.010	0.021	3	−0.108	0.030	3	−0.118	0.036	0.003
6	24	1.00	17.69	0.020	0.031	3	−0.080	0.026	2	−0.100	0.040	0.006
7	48	1.00	28.10	0.034	0.024	3	−0.068	0.012	2	−0.102	0.027	0.008
9	168	1.00	47.59	0.052	0.022	3	−0.040	0.021	2	−0.093	0.030	0.002
Variable adsorption in equilibrium												
10	48	0.50	5.08	0.019	0.009	2	−0.112	0.006	3	−0.131	0.011	0.013
11	48	0.75	10.56	0.034	0.014	2	−0.088	0.020	3	−0.122	0.025	0.021
12	48	1.00	15.52	0.035	0.011	2	−0.086	0.009	3	−0.122	0.014	0.017
13	96	1.25	20.72	0.044	0.004	2	−0.070	0.022	3	−0.115	0.022	0.020
14	96	1.50	20.15	0.052	0.044	2	−0.075	0.010	3	−0.126	0.045	0.026
15	96	1.75	24.29	0.041	0.022	2	−0.063	0.031	3	−0.104	0.038	0.023
16	144	2.00	30.18	0.039	0.055	2	−0.060	0.014	3	−0.083	0.014	0.009
17	144	2.25	33.29	0.058	0.011	3	−0.059	0.003	3	−0.117	0.011	0.019
18	144	2.50	38.28	0.045	0.021	3	−0.054	0.005	3	−0.100	0.021	0.007

2×SD calculated from replicate analyses of the same solution on the mass spectrometer
Expt. = Experiment number
n = Number of replicate analyses of same solution
Fhy = Ferrihydrite
Prop. uncert. = Propagated uncertainty via adding uncertainties in quadrature
Mass balance = Isotopic composition of the bulk experiment calculated after Equation 8

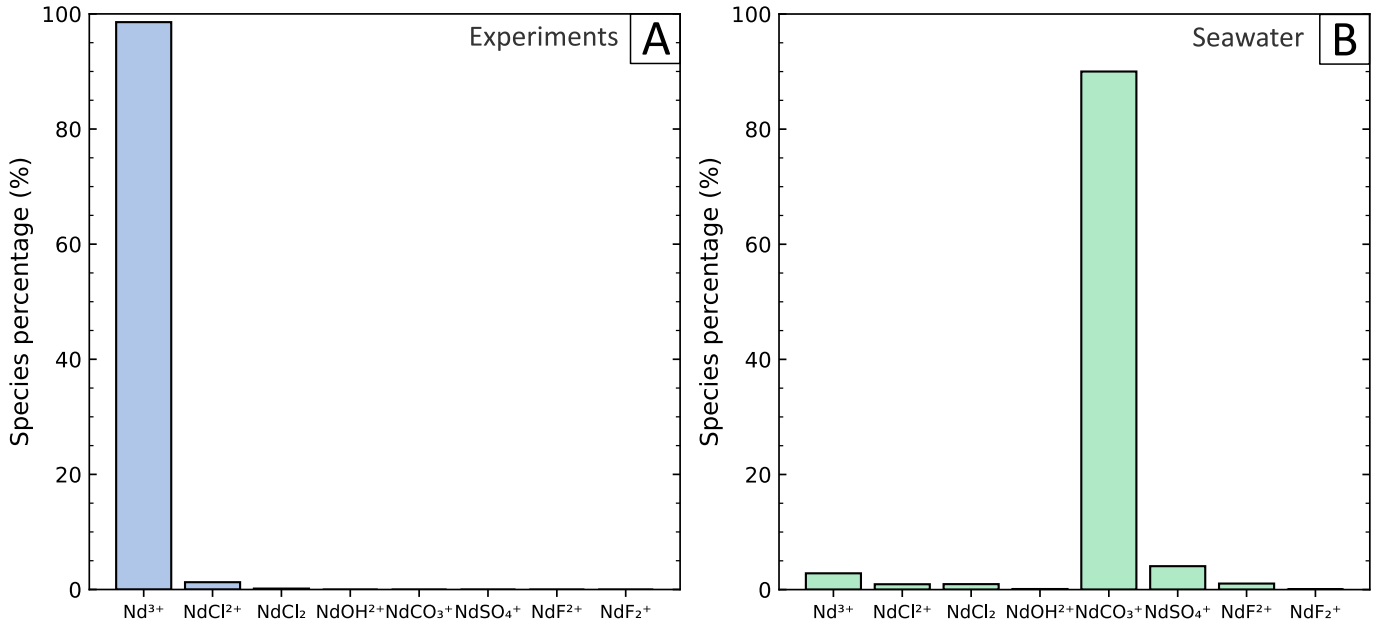

Figure 1. Neodymium speciation in (a) the experiment solution and (b) simplified seawater derived from thermodynamic modelling. Only shown are species that account for > 0.01 % of speciation in either solution.

(2×SD; n = 8) and 0.134 ± 0.014 ‰ (2×SD; n = 8), respectively, which agree within uncertainty with previously reported values of −0.095 ± 0.019 ‰ and 0.113 ± 0.019 ‰, respectively (Kaufmann and McCoy-West, 2025; McCoy-West et al., 2020b). The geostandard BHVO-2 was also measured during the session, which yielded a δ^{146}Nd value of −0.024 ± 0.014 ‰ (95 % se; n = 1) which agrees within uncertainty of reported values of −0.030 ± 0.014 ‰ (McCoy-West et al., 2021) and −0.030 ± 0.033 ‰ (Bai et al., 2022). The HPS standard used as Nd dopant in the experiments here is identical to that characterised by Kaufmann and McCoy-West (2025) which has an isotopic composition of δ^{146}Nd = 0.010 ± 0.023 ‰ (2×SD; n = 28). Radiogenic ^{143}Nd/^{144}Nd and stable ^{148}Nd/^{144}Nd are calculated following double spike deconvolution. All experimental phases (i.e. solids and liquids) display mass-dependent behaviour (Fig. S1 in the Supplementary Material) and ^{143}Nd/^{144}Nd compositions within uncertainty of the HPS Nd dopant (Fig. S2) confirming the robustness of the measurements. Procedural blanks for experiments were 1.17 ng Nd on average (n = 6) and are considered negligible.

2.3.2 Isotopic analysis of seawater samples

Isotopic measurements of the seawater samples were undertaken in the Arthur Holmes Geochemistry Laboratories at Durham University in 2018. The pH of the seawater was adjusted to ca. 3.5 and the samples (ca. 20 ng natural Nd) were subsequently spiked (50 % sample; 50 % spike) with the same ^{145}Nd-^{150}Nd double spike. The water samples were then left to equilibrate with the spike for either 5, 10 or 15 days. The REE were then concentrated by liquid-liquid extraction following the techniques outlined by Pahnke et al. (2012). Briefly, the water was pumped through two coupled Sep-Pack C18 cartridges, each filled with 300 mg of a mixture of 65 % bis(2-ethylhexyl)hydrogen phosphate (HDEHP) and 35 % 2-ethylhexyl dihydrogen phosphate (H_2MEHP), at a speed of 20 mL/min. Barium was first eluted from the cartridges using 5 mL of 0.01 mol/L HCl, and the REE were then collected in 35 mL of 6 mol/L HCl. Following Nd separation by ion exchange chromatography as described in Section 2.3.1, Nd isotope measurements were performed using a Thermo Fisher Scientific® TritonPlus thermal ionisation mass spectrometer (TIMS) at Durham University. Neodymium was measured as a metallic ion in static collection mode using eight faraday cups with 10^{11} Ω resistors, with ^{147}Sm monitored to correct for isobaric interferences on ^{144}Nd, ^{148}Nd and ^{150}Nd. Each analysis usually comprised 400-600 cycles of data acquisition (8 s per integration) aiming for a minimum voltage of 0.2 V on ^{146}Nd. Data was processed as described in McCoy-West et al. (2020b). Analytical blanks during this period were ca. 16 pg (n = 3), making them negligible. Long-term analytical uncertainties from 200 ng natural Nd loads (which produce ca. 2–4 V on ^{146}Nd for the analysis duration) are ± 0.015 ‰ for δ^{146}Nd and ± 0.000011 for ^{143}Nd/^{144}Nd (McCoy-West et al., 2020b). Therefore, due to the worse counting statistics at lower voltages, here conservative long-term analytical uncertainties on seawater analyses are considered to be ± 0.045 ‰ for δ^{146}Nd and ± 0.000015 ^{143}Nd/^{144}Nd. Due to the low measurement signals (≤ 0.07 V on ^{148}Nd), δ^{148}Nd values (which are calculated outside the double spike deconvolution) are not considered accurate and are therefore not presented for these analyses.

Radiogenic Nd isotope compositions are reported as deviation from the chondritic uniform reservoir (CHUR) using $(^{143}Nd/^{144}Nd)_{CHUR} = 0.512638$ (Hamilton et al., 1983; Jacobsen and Wasserburg, 1980):

$$\varepsilon_{Nd} = \left[\frac{(^{143}Nd/^{144}Nd)_{sample}}{(^{143}Nd/^{144}Nd)_{CHUR}} - 1 \right] \times 10^4 \qquad (3)$$

Table 2. Neodymium concentrations and isotopic compositions in seawater samples.

Sample name	Equilibration (days)	^{146}Nd (V)	Nd (pg/mL)	^{143}Nd/^{144}Nd	ε_{Nd}	δ^{146}Nd (‰)	Cycles (n)
SH1-A	15	0.403	3.75	0.512089 ± 7	-10.71	0.311 ± 0.016	407
SH1-B	Unspiked	0.241	-	0.512065 ± 5	-11.18	-	400
SH1-D	5	0.248	3.74	0.512067 ± 9	-11.14	0.270 ± 0.018	418
SH1-E	10	0.183	4.16	0.512092 ± 12	-10.64	0.338 ± 0.023	365
SH1-G	10	0.400	3.83	0.512050 ± 6	-11.46	0.327 ± 0.013	576
Average			3.87 ± 0.39	0.512073 ± 35	-10.99 ± 0.69	0.312 ± 0.060	

Individual measurement uncertainties are 95 % se
Uncertainties on averages are 2×SD
^{146}Nd (V) represents the average signal intensity during the TIMS analysis using a 10^{11} Ω resistor.

Table 3. Parameters obtained from a molecular dynamics simulation of Nd on ferrihydrite from this study compared with extended X-ray absorption fine structure experimental data.

Method	CN(O)	Nd-O (Å)	σ^2 (Nd-O) (Å^2)	CN(Fe)	Nd-Fe (Å)	σ^2 (Nd-Fe) (Å^2)	Reference
EXAFS (one oxygen shell fit)	6.5 ± 1.1	2.484 ± 0.013	0.011	1.3 ± 0.4	3.342 ± 0.064	0.010	Nakada et al. (2013b)
EXAFS (two oxygen shell fit)	0.8 ± 0.4	2.279 ± 0.043	0.010	1.4 ± 0.6	3.356 ± 0.024	0.010	Nakada et al. (2013b)
	7.1 ± 0.6	2.494 ± 0.007	0.010				
MD	8.0	2.489	0.014	1.9	3.665	0.017	This study

CN = Coordination number
σ^2 = Debye-Waller factor
EXAFS = Extended X-ray Absorption Fine Structure
MD = Molecular Dynamics

2.4 Ab initio molecular dynamics simulations

Ab initio molecular dynamics (MD) simulations were performed using the CP2K/QUICKSTEP code with mixed gaussian and planewave basis sets (Kühne et al., 2020; VandeVondele et al., 2005). The DZVP-MOLOPT-GTH basis set (VandeVondele and Hutter, 2007) was used with 4f in core pseudopotentials for REE. The ferrihydrite structure after Michel et al. (2007) was used for the ferrihydrite slab model. The simulation was performed on the (100) surface which contains singly-coordinated ≡Fe-OH surface groups and it is therefore representative for reactive surface sites on ferrihydrite such as (101) and (10$\bar{1}$). The (001) surface of ferrihydrite is not reactive as it only possesses doubly- and triply-coordinated surface oxygens (Hiemstra, 2013). The (100) surface was transformed to the (001) surface in VESTA (Momma and Izumi, 2011) using the transformation matrix:

$$\begin{pmatrix} 0 & 0 & -1 \\ -2 & 0 & 0 \\ 0 & -1 & 0 \end{pmatrix}$$

A 2×1×1 supercell was then created to obtain a slab with ca. 6 Å thickness. The supercell was then converted to an orthorhombic system which is more efficient in CP2K. All surface oxygens were protonated to get a final unit cell with the composition $Fe_{20}O_{48}H_{33}$. A vacuum space of ca. 20 Å was added along the c-axis and filled with 62 water molecules. The final unit cell had cell parameters of a = 11.86 Å, b = 9.13 Å, and c = 25.81 Å. Spin polarisation was done with alternating spin directions of Fe along the original c-axis (b-axis in transformed supercell; Pinney et al., 2009). The modelled slab had a total charge of −3 and the simulation box a net charge of 0 by adding a trivalent Nd ion. Trivalent neodymium in aqueous solution was modelled in a cubic box of 15.24 Å side length with 111 waters and 3 Cl^- ions for charge balance. The two simulation boxes had a density of ca. 1 g/cm^3. A plane-wave cutoff of 400 Ryd was used with the PBE exchange functional (Perdew et al., 1996) and Grimme's D3 dispersion correction (Grimme et al., 2010). The Nd on ferrihydrite simulation was performed over 40 000 steps (0.5 fs per step) which represents a duration of 20 ps. The Nd in aqueous solution simulation was performed over 80 000 steps. The system was simulated in the NVT ensemble in which number of atoms, volume, and temperature were kept constant. The temperature was maintained using a Nosé thermostat (Nosé, 1984). The simulations were performed at a temperature of 298.15 K (25 °C). Radial distribution functions (RDF), coordination numbers (CN), and Nd-O bond lengths were calculated using Visual Molecular Dynamics (VMD; Humphrey et al., 1996). The Nd-O bonds were monitored to assess the equilibration time for the simulation. The time required to reach equilibration was removed before RDF calculations. The Debye-Waller factor (σ^2) was calculated after Campbell et al. (1999):

$$\sigma^2 = \frac{1}{N} \times \sum_{i=1}^{N} (R_i - R_{average})^2 \quad (4)$$

where N is the number of simulation steps, R_i is the Nd-O bond length at step i, and $R_{average}$ is the average Nd-O bond length throughout the simulation without the equilibration time.

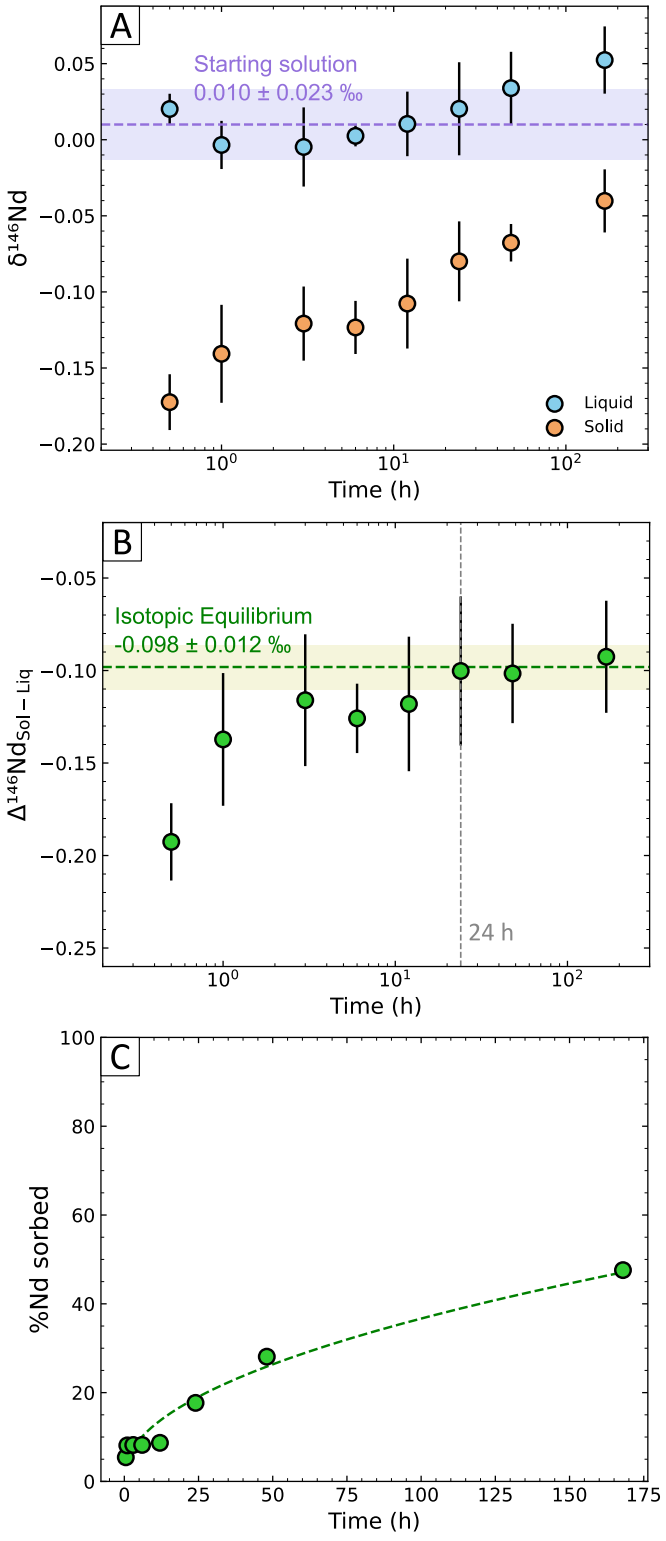

Figure 2. Results of time series experiments. (a) The liquid phase is enriched in ^{146}Nd compared to the solid phase throughout the series. The initial HPS Nd dopant has a δ^{146}Nd composition of 0.010 ± 0.023 ‰ (2×SD) shown as the shaded field with the average a dashed line (Kaufmann and McCoy-West, 2025). (b) The difference in isotopic composition between solid and liquid phase remains constant within a 95 % se interval (shaded field) of the samples with a duration of ≥ 24 h demonstrating isotopic equilibrium is achieved. (c) Nd is rapidly sorbed in the first 48 h followed by a slower uptake.

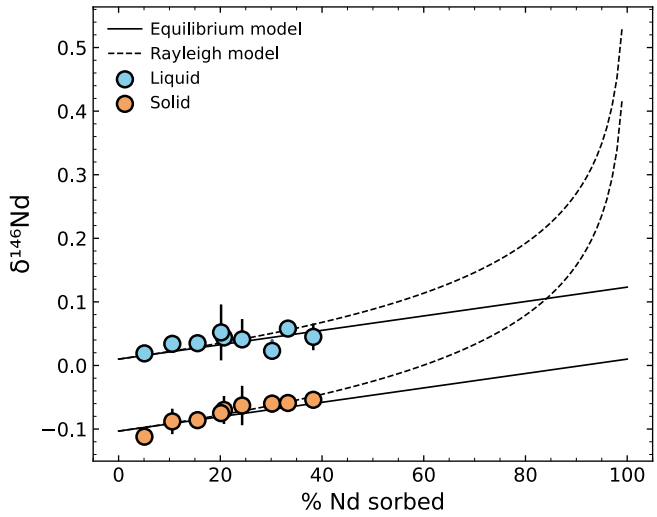

Figure 3. Experiments with variable amount of sorbed Nd display equilibrium fractionation. Due to the incomplete adsorption of Nd on the ferrihydrite surface, the fractionation in open isotopic exchange cannot be confirmed.

3 Results

3.1 Solution chemistry

The XRD pattern of the synthesized mineral shows two characteristic humps above background at 35° and 62° 2θ which confirms a successful synthesis of 2-line ferrihydrite (Fig. S3; Drits et al., 1993). Speciation modelling of the experimental solution shows that free Nd^{3+} is the predominant species (98.57 %) with chloride complexes $NdCl^{2+}$ (1.27 %) and $NdCl_2^+$ (0.16 %) in minor abundances (Fig. 1). In the simplified seawater, however, $NdCO_3^+$ is by far the most abundant species (90.01 %; Fig. 1).

3.2 Experimental Nd isotope compositions

An overview of conducted experiments and isotopic compositions are given in Table 1 and Nestmeyer et al. (2026). Iron concentrations in the liquid phase were < 0.023 % of the total Fe concentration in the experiment demonstrating that solid and liquid phases were successfully separated. The purpose of the time series experiments was to assess kinetic effects, and the duration required to achieve isotopic equilibrium.

To determine isotopic equilibrium, we calculated a $\Delta^{146}Nd_{Sol\text{-}Liq}$ 95 % confidence interval (i.e. how well constrained the mean value) of the experiments with a duration of ≥ 24 h, which gives a value of −0.098 ± 0.012 ‰. All experiments show identical $\Delta^{146}Nd_{Sol\text{-}Liq}$ within the 95 % se interval between 24 and 168 h. (Fig. 2a, b). This demonstrates that isotopic equilibrium is achieved after at least 24 h. Prior to isotopic equilibrium, the solid phase is more enriched in ^{144}Nd, showing that kinetic effects enrich lighter Nd on ferrihydrite. Uptake of Nd was rapid initially with 8 % adsorbed after 6 h, 18 % after 24 h, 28 % of Nd was adsorbed within 48 h and 48 % after one

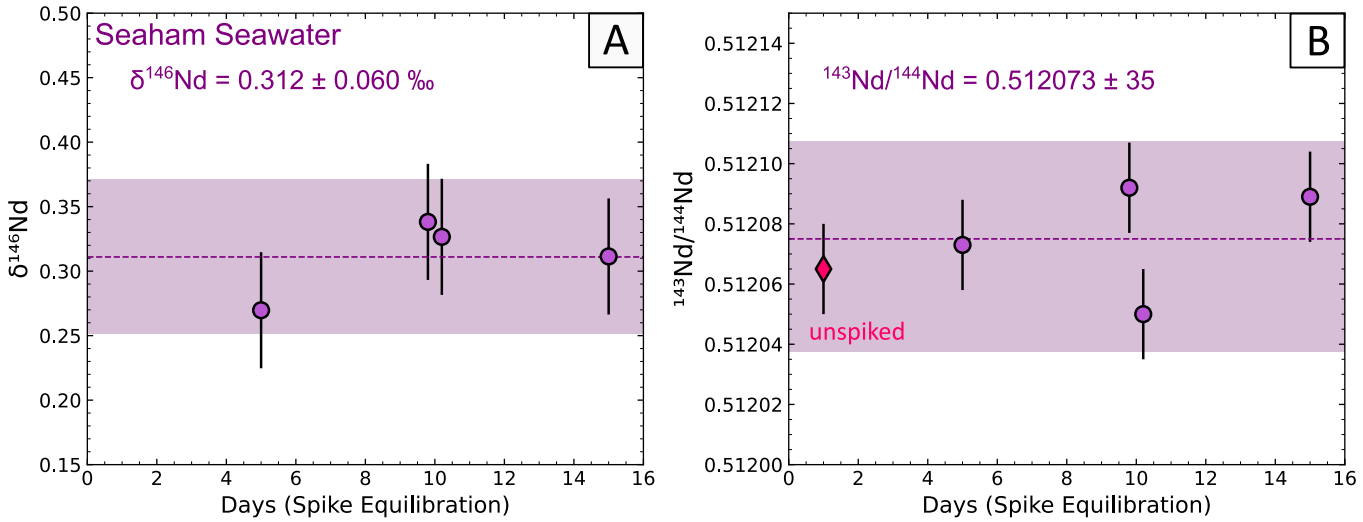

Figure 4. Variable spike-sample equilibration time for Seaham seawater samples. (a) Stable Nd isotope composition does not change with an equilibration time longer than five days. (b) Radiogenic composition of unspiked seawater analysis agrees with the spiked analyses within uncertainty. Shaded fields represent the average (dashed line) ±2×SD. Individual data points are plotted with a conservative long-term uncertainty. Due to the small amount of Nd processed larger long-term uncertainties than previous works are prudent (±0.000015 for $^{143}Nd/^{144}Nd$ and ±0.045 ‰ for $\delta^{146}Nd$; see Section 2 Methodology).

week (Fig. 2c). Sorption becomes slower with increasing experiment duration which agrees with findings in previous studies (Barling and Anbar, 2004; Brennecka et al., 2011; Dong and Wasylenki, 2016; Wasylenki et al., 2008). The constant offset in isotopic composition between aqueous and solid phase after 24 h despite ongoing Nd uptake demonstrates that elemental equilibration occurred more slowly. Isotopic equilibrium is not influence by elemental uptake instead it is controlled by differences in bonding environment between the aqueous and surface complexes, which remain constant after kinetic effects are overcome (cf. Goldberg et al., 2009).

The purpose of the second set of experiments was to use variable amounts of ferrihydrite stock solution (0.5–2.5 mL) and different reaction times (48–144 h) to obtain experiments with variable amounts of sorbed Nd. Percentages of adsorbed Nd range from 5 to 38 % (Table 1). All of these experiments ran for at least 48 h and form parallel trends confirming that the experiments were in isotopic equilibrium (Fig. 3). The equilibrium fractionation factor (α-factor) was then calculated following:

$$\alpha_{Solid-Liquid} = \frac{1000 + \delta^{146}Nd_{Solid}}{1000 + \delta^{146}Nd_{Liquid}} \quad (5)$$

which yielded an average value of 0.999886 ± 0.000030 which corresponds to an average $10^3 \ln\alpha$ value of −0.113 ± 0.030 which is equal to $\Delta^{146}Nd_{Sol\text{-}Liq}$. This value is very similar and within uncertainty of the value obtained in the timeseries experiments. Equilibrium and Rayleigh fractionation models were constructed using the obtained average α-factor following:

1) Equilibrium Model (isotopic exchange):

$$\delta^{146}Nd_{Liquid} = \frac{\delta^{146}Nd_{HPS} - 1000 \times f_{sorbed} \times (\alpha_{Solid-Liquid} - 1)}{1 - f_{sorbed} + (f_{sorbed} \times \alpha_{Solid-Liquid})} \quad (6)$$

2) Rayleigh Model (no isotopic exchange):

$$\delta^{146}Nd_{Liquid} = (1000 + \delta^{146}Nd_{HPS}) \times (1 - f_{sorbed})^{\alpha_{Solid-Liquid}-1} - 1000 \quad (7)$$

where $\delta^{146}Nd_{HPS}$ represents the isotopic composition of the dopant (0.010 ± 0.023 ‰). The datapoints follow the parallel equilibrium curves with both phases becoming systematically isotopically heavier depending on the amount of sorbed Nd (Fig. 3). Given incomplete adsorption of Nd was achieved at 144 h, an open exchange model cannot be confirmed here.

The fraction of Nd in the two phases and their isotopic composition was then used to recalculate via mass balance the composition of the original HPS Nd stock solution. An offset outside uncertainty (2 times standard deviation) would indicate significant contamination or precipitation of Nd that was not accounted for. Mass balancing was calculated using:

$$\delta^{146}Nd_{Mass\ balance} = (\delta^{146}Nd_{Liquid} \times f_{Liquid}) + (\delta^{146}Nd_{Solid} \times f_{Solid}) \quad (8)$$

No experiments fell outside of the composition of the HPS stock solution (0.010 ± 0.023 ‰; Kaufmann and McCoy-West, 2025).

3.3 Seawater Nd isotope compositions

The seawater samples (n = 4) have $\delta^{146}Nd$ compositions between 0.270 ± 0.018 ‰ and 0.338 ± 0.023 ‰ and are shown in Table 2. The average $\delta^{146}Nd$ composition is 0.312 ± 0.060 ‰ (2×SD). Samples were equilibrated with the spike for 5, 10, or 15 days and show a homogeneous composition within 2 times the standard deviation (Fig. 4a, b). No difference in $\delta^{146}Nd$ and $^{143}Nd/^{144}Nd$

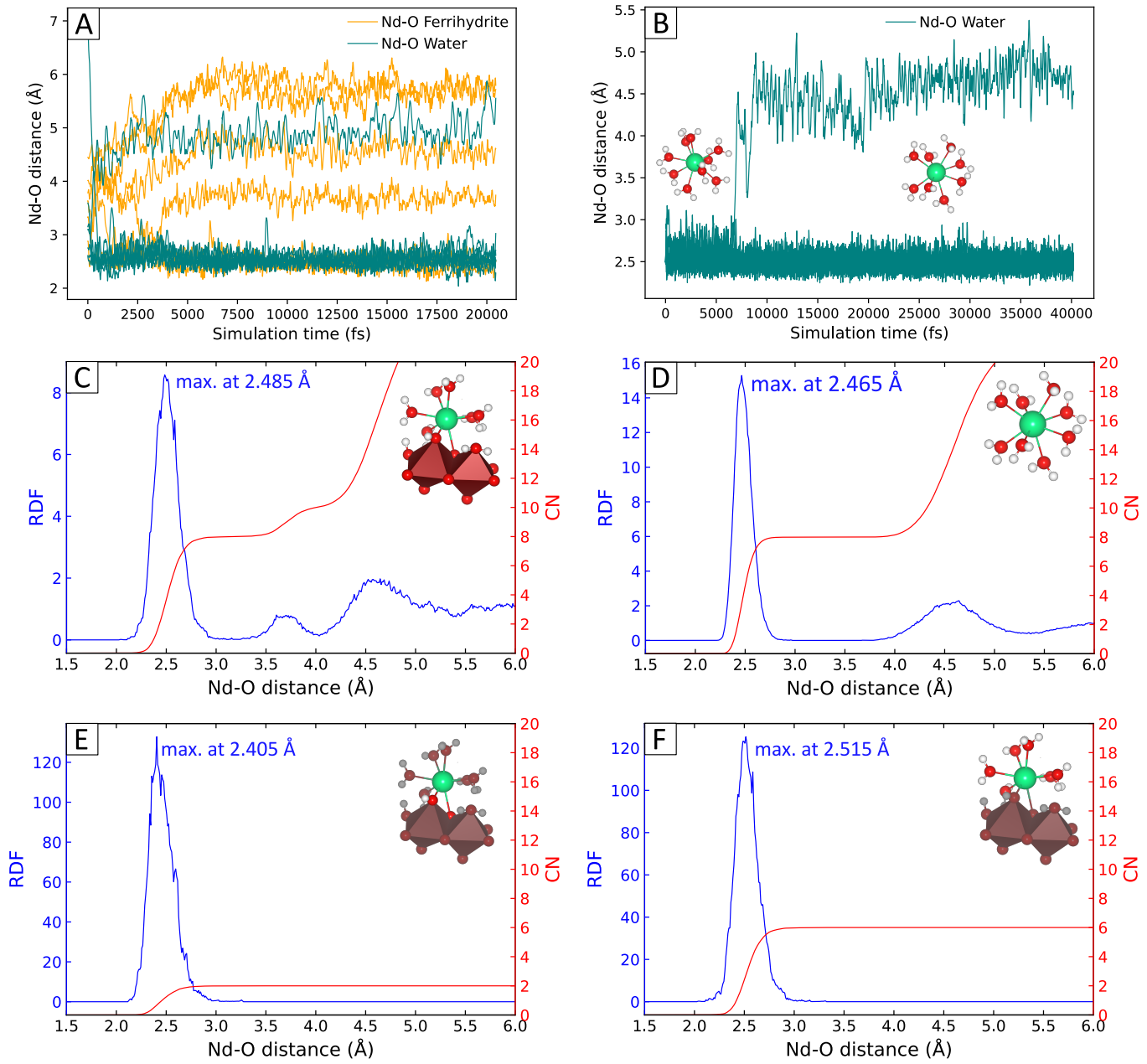

Figure 5. (a) Nd-O bond distances in the first shell of Nd on ferrihydrite throughout the simulation time. The first 5 ps were excluded from further analyses to make sure that the system is equilibrated. (b) Nd-O bond distances of Nd in aqueous solution with a $Nd(H_2O)_9$ starting geometry. Following ca 8.5 ps, the system is stable in a $Nd(H_2O)_8$ configuration. Radial distribution function (RDF) and coordination number (CN) over the equilibrated simulation time are shown for (c) Nd on ferrihydrite, and (d) Nd in aqueous solution. RDF for water oxygens and ferrihydrite surface oxygens are shown separately in (e) and (f), respectively.

composition between the different times used for sample-spike equilibration within analytical uncertainties confirms that equilibration was achieved in all samples. The concentration of Nd in the Seaham seawater varies from 3.74 to 4.16 pg/mL (Table 2). One aliquot was processed unspiked and produced a $^{143}Nd/^{144}Nd$ isotope composition of 0.512065 ± 5. The aliquots processed using a double spike produced $^{143}Nd/^{144}Nd$ values within uncertainty of this value (Fig. 4b). The radiogenic isotope compositions (ε_{Nd} = ca. −11 to −10; Table 2) are consistent with regional Nd expectations (average $\varepsilon_{Nd} = -12 \pm 2$ for the Atlantic Ocean; Piepgras and Wasserburg, 1980).

3.4 Molecular dynamics simulation

Equilibration of Nd on ferrihydrite and Nd in aqueous solution simulations was achieved after approximately 5000 and 8500 fs, respectively (Fig. 5a, b). No exchange of oxygen atoms in the first coordination shell was observed for the remaining simulation of ca. 15 000 and 31 500 fs, respectively. Figure 5c and d show the radial distribution function (RDF) and coordination number (CN) of the simulation after 5000

and 8500 fs when the system was equilibrated. The observed coordination number and average Nd-O bond length of Nd on the ferrihydrite surface are 8.0 and 2.485 Å, respectively. The coordination of Nd on ferrihydrite obtained in this study is shown in Table 3 and is compared with experimental data from Nakada et al. (2013b). The observed coordination number of 8.0 is higher than what was found using EXAFS at 6.5 ± 1.1. However, a two oxygen shell fit of the experimental EXAFS data is in good agreement with the results from the MD simulation presented here (0.8 ± 0.4 and 7.1 ± 0.6, respectively). The experimental EXAFS Nd-O bond length of 2.484 ± 0.013 Å (Nakada et al., 2013b) agrees within uncertainty with the value derived from the MD simulation (2.485 Å). The observed surface complex is an inner-sphere bidentate edge sharing complex which is hydrated by 6 additional water molecules (Fig. 6a, b). Comparison of the Nd-Fe distance with experimental EXAFS data (Nakada et al., 2013b) confirms an inner-sphere complexation that is mononuclear (Nd-Fe coordination number < 2.0). The Nd-O bonds with surface oxygens are shorter (2.405 Å) compared to bonds with water oxygens (2.515 Å; Fig. 5e, f). A compilation of the coordination of Nd in aqueous solution observed in 11 experimental studies is shown in Table 4. Observed coordination numbers range from 8 to 12 with an average of 9.4 ± 2. The Nd-O bond lengths range from 2.487 to 2.526 Å with an average of 2.490 ± 0.061 Å. In our MD simulation, Nd in aqueous solution has a CN of 8.0 with an average Nd-O bond length of 2.465 Å (Fig. 5d), these values are slightly lower than the average experimental values of 9.4 ± 2 and 2.490 ± 0.061 Å, respectively, but agree within analytical uncertainties. The Debye-Waller factors (σ^2) in Table 3 and 4 represent the average σ^2 for all Nd-O and Nd-Fe in the first coordination shell and are compared with experimental data. For Nd on ferrihydrite, the Debye-Waller factor of 0.014 Å^2 is significantly higher than the single experimental determination of 0.010 Å^2 (Table 3). For Nd in aqueous solution, the Debye-Waller factor derived from the MD simulation is 0.008 which is in good agreement with EXAFS data (0.009 ± 0.001 Å^2).

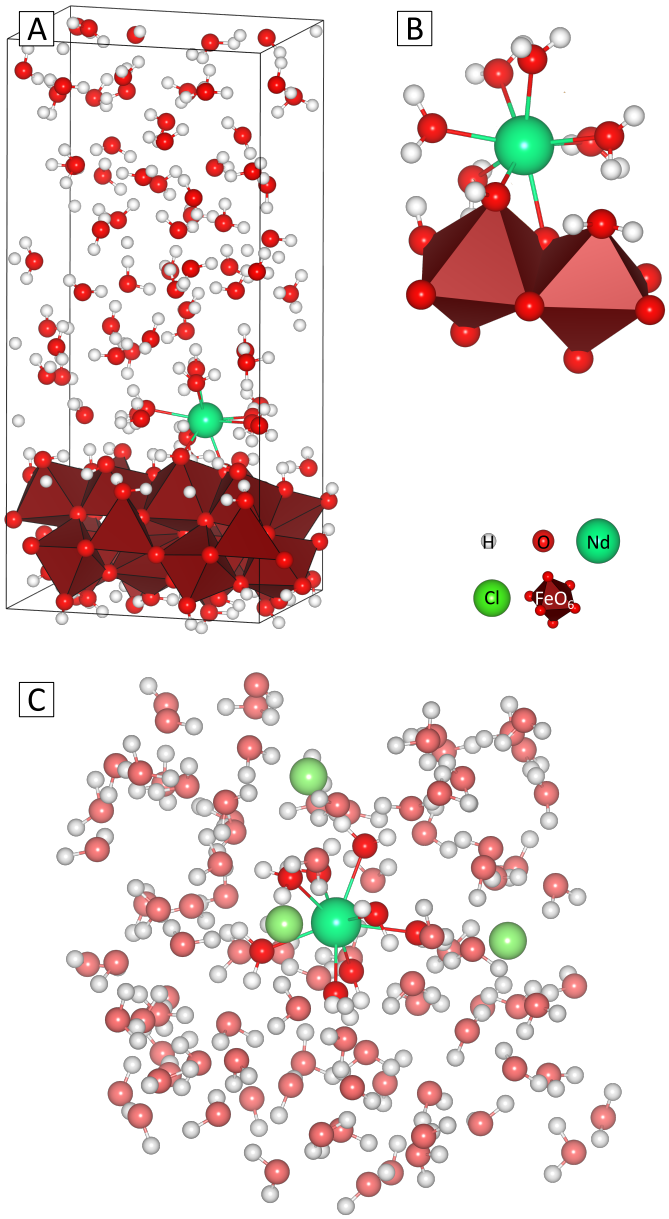

Figure 6. Nd complexes observed in the molecular dynamics simulations. (a) Molecular dynamics simulation box of Nd on ferrihydrite. (b) Observed bidentate mononuclear edge-sharing surface complex. (c) Nd in aqueous solution box with three Cl^- anions for charge balance.

4 Discussion

4.1 Coordination of Nd on ferrihydrite and isotope fractionation

Generally, equilibrium mass-dependent isotope fractionation is driven by differences in vibrational energies between bonding environments (Bigeleisen and Mayer, 1947; Urey, 1947). As the bonding environment changes between Nd^{3+} in aqueous solution and Nd^{3+} adsorbed on the surface of ferrihydrite, isotopes will fractionate between the aqueous and surface complex. Therefore, both phases should have different Nd isotope compositions. Equilibrium mass-dependent isotope fractionation is generally related to changes in the coordination environment of the metal. Higher oxidation states, shorter bonds, and lower coordination numbers form stiffer bonds which favour heavier isotopes (Schauble, 2004). However, rarely adsorption processes that do not follow these rules have been found. For example, Cu^{2+} sorbed on birnessite has shorter bonds and a lower coordination number than in aqueous solution has been observed to be isotopically lighter on the mineral surface. Thus, the qualitative idea of the isotope fractionation based on changes in bond lengths and coordination number is not always followed (Ijichi et al., 2018; Little et al., 2014; Sherman and Little, 2020). Correlations of bond length or coordination numbers with the magnitude of isotope fractionation reported in ab initio studies on aqueous complexes or crystals are also only moderate (Fujii et al., 2014; Huang et al., 2019; Schauble, 2011; Yang et al., 2015). Consequently, those parameters

Table 4. Coordination parameters of Nd in aqueous solution from experimental literature data.

Method	CN(O)	Nd-O length (Å)	σ^2 (Å^2)	Reference
EXAFS	10	2.514	0.009	Mayanovic et al. (2009)
EXAFS	9.5	2.49		Allen et al. (2000)
EXAFS	9	2.488	0.008	Ishiguro et al. (2002)
EXAFS	9.5	2.51	0.008	Yamaguchi et al. (1988)
EXAFS		2.49		Persson et al. (2008)
EXAFS	12	2.48	0.008	Solera et al. (1995)
EXAFS	10	2.487	0.010	Nakada et al. (2013b)
EXAFS	9.1	2.526	0.009	Shiery et al. (2021)
ND	8.4	2.48		Narten and Hahn (2002)
XRD	8	2.41		Steele and Wertz (1977)
XRD	8.9	2.513		Habenschuss and Spedding (1979)
Average Expt.:	9.4 ± 2	2.490 ± 0.061	0.009 ± 0.001	
MD	8	2.465	0.008	This study

CN = Coordination number
σ^2 = Debye-Waller factor
EXAFS = Extended X-ray Absorption Fine Structure
ND = Neutron Diffraction
XRD = X-Ray Diffraction
MD = Molecular Dynamics
Uncertainties shown are 2×SD

are only qualitative indicators for isotope fractionation and are not completely reliable.

There has been a traditional view that metal cations (e.g. Zn, Cu) are isotopically heavier on mineral surfaces due to their lower coordination number and shorter bonds compared to their aqueous complexes. Unless the metals form oxyanions in aqueous solution (e.g. Mo, Se) which usually change from tetrahedral coordination in aqueous solution to octahedral coordination on mineral surfaces and are therefore isotopically lighter in surface complexes (Balistrieri et al., 2008; Barling and Anbar, 2004). However, notwithstanding these complications, at present enrichment of lighter isotopes on ferrihydrite has been observed for most metals (e.g. Ni, Cd, and Sr) which keep their octahedral coordination in aqueous solution during sorption onto the mineral surface (Liu et al., 2024; Wasylenki et al., 2015; Yan et al., 2021). The enrichment of lighter isotopes on mineral surfaces when keeping the same coordination number as in the aqueous solution is generally attributed to the higher distortion in the surface complex due to the presence of complexed surface ≡Fe-OH groups compared to the more symmetrical complex in aqueous solution. The REE and yttrium form a trigonal tricapped prismatic (9-fold) or square antiprismatic (8-fold) atomic coordination in aqueous solution (Brugger et al., 2016; Guan et al., 2020) which is different from the metal cations studied in the past.

While previous experimental data shows a lower CN in the surface complex than in the aqueous complex (Table 3, 4), this is not observed in the MD simulations where both complexes have a CN of 8.0. The experimental average bond length of Nd in aqueous solution (2.490 ± 0.061 Å; Table 4) is indistinguishable from the experimental Nd-O bond length on ferrihydrite (2.484 ± 0.013 Å; Table 3) within analytical uncertainties, and the Nd-O bond length on ferrihydrite obtained using MD simulation herein (2.485 Å; Table 3). However, the Nd-O bond length in the MD simulation of Nd in aqueous solution is 2.465 Å which is shorter than Nd-O on ferrihydrite which suggests preferential enrichment of heavier isotopes in the aqueous complex which agrees with the adsorption experiments from this study. However, the PBE exchange functional used here tends to over-structure water which could result in a slight underestimation of the CN and Nd-O bond length of the aqueous complex (Mei et al., 2020), and it cannot be stated with confidence that the aqueous complex has shorter bonds than the surface complex. More importantly, the Nd-O Debye-Waller factor of Nd in aqueous solution in the MD simulation is 0.008 Å^2 which agrees with experimental data (0.009 ± 0.001 Å^2; Table 4) and is considerably smaller than in the surface complex (σ^2 = 0.014 Å^2; Table 3). A smaller Nd-O Debye-Waller factor indicates stiffer bonds and, therefore, also enrichment of heavier isotopes in the aqueous complex which agrees with the results from the adsorption experiments. The difference in bond stiffness is less clear in the experimental data where the surface complex has a Debye-Waller factor of 0.011 Å^2 or 0.010 Å^2 derived from one oxygen shell fit and two oxygen shell fit, respectively. The MD simulation of the surface complex also shows a significantly higher Nd-Fe Debye-Waller factor than the experimental data (0.017 Å^2 versus 0.010 Å^2). The ab initio simulation, therefore, suggests Nd is more loosely bound to the ferrihydrite surfaces than the EXAFS data.

The observed isotope fractionation of −0.113 ‰ is relatively large for a heavy element like Nd without a change in oxidation state. For comparison, the fractionation observed in low temperature systems like weathering profiles and marine sediments ranges from δ^{146}Nd = −0.152 to 0.271 ‰ (range of 0.423 ‰) (Bai et al., 2025, 2023; Kaufmann and McCoy-West, 2025). Similarly, isotope fractionation of ^{142}Ce/^{140}Ce in low temperature systems

like soil and marine sediments has been shown to span a similar range ($\delta^{142}Ce = -0.277$ to 0.210 ‰; range of 0.487 ‰) (Bai et al., 2024; Li et al., 2023, 2025; Zhang et al., 2026). Given that outer-sphere complexation is accompanied by very limited isotope fractionation because of the limited change in coordination and distortion (e.g. Zhou et al., 2022), the isotope fractionation observed in the experiments here supports the formation of inner-sphere surface complexes found in the MD simulation. The MD simulation presented here, however, only explores one potential local energetic minimum of Nd on ferrihydrite. Other potential surface complexes might cause different isotope fractionations. However, given that the results from MD simulation agree well with EXAFS data, a significant proportion of a different surface complex with a vastly different coordination environment is unlikely.

Elements that change their oxidation state between aqueous and surface complex are isotopically heavier in the higher oxidation state which is usually the surface complex (Nielsen et al., 2013). Because Nd only occurs in the 3+ oxidation state in terrestrial environments, an isotope fractionation effect driven by oxidation can be excluded here. In addition, for REE, the mass-independent nuclear field shift effect also provides an important contribution to equilibrium isotope fractionation (Nestmeyer and McCoy-West, 2025; Schauble, 2023, 2024). However, the proportion of the field shift of the total isotope fractionation is not substantial without a change in oxidation state (Nestmeyer and McCoy-West, 2026). For example, the mass-dependent fractionation among aqueous complexes of Ce^{3+} reaches values of 0.332 ‰ at 25 °C, whereas the nuclear field shift fractionation only reaches 0.019 ‰ without redox change (Nestmeyer and McCoy-West, 2025). Therefore, a similar magnitude can be expected for Nd.

Overall, isotope fractionation of Nd on ferrihydrite is best explained by the formation of an inner-sphere complex and stiffer bonds in the aqueous complex compared to the surface complex which favours heavier isotopes. The nuclear field shift effect or a change in oxidation state does not play a role.

4.2 Comparison with natural samples of seawater and seafloor sediments

The isotope fractionation between metals in aqueous solution and surfaces of birnessite and ferrihydrite observed in adsorption experiments is generally consistent with the difference in isotopic composition between seawater and Fe-Mn-crusts observed in natural samples for Cu, Zn, Sr, and Mo (Barling and Anbar, 2004; Ijichi et al., 2018; Juillot et al., 2008; Little et al., 2014; Liu et al., 2024). Stable Nd isotopes in marine sediments and aqueous systems have been little studied, although the isotope fractionation can be expected to be higher in these systems compared to the limited isotope fractionation observed in high-temperature systems like igneous rocks (Bai et al., 2022; McCoy-West et al., 2017, 2021, 2022) because of the proportionality of mass-dependent fractionation to $1/T^2$ (Bigeleisen and Mayer, 1947). A recent study by Bai et al. (2025) provides some data of Fe-Mn (hydr)oxides in marine sediments. The data are shown in Figure 7 together with data from seawater samples from this study. Clearly, natural waters are isotopically heavier than Fe-Mn oxides which is reflected in the adsorption experiments here. The difference in isotopic composition between natural seawater and Fe-Mn (hydr)oxides is 0.357 ‰ on average which is larger than the fractionation of 0.113 ‰ found in the adsorption experiments here. However, Nd in seawater is primarily complexed with CO_3^{2-} (De Baar et al., 1991; Turner et al., 1981) while free Nd^{3+} is the predominant species in the adsorption experiments (Fig. 1). As shown by Nestmeyer and McCoy-West (2025), $NdCO_3^+$ complexes are heavier than free Nd^{3+} by 0.107 ‰ at 25 °C which can explain a much larger magnitude of fractionation in natural samples.

In order to quantify the isotope fractionation that can be expected between seawater and ferrihydrite, reduced partition function ratios ($10^3 \ln\beta$) of Nd in the solution used in the adsorption experiments and in seawater were calculated using:

$$10^3 \ln\beta = \sum 10^3 \ln\beta_i \times f_i \quad (9)$$

where $10^3 \ln\beta_i$ is the reduced partition function ratio of species i from Nestmeyer and McCoy-West (2025), and f_i is the proportion of species i as a fraction of unity from the PHREEQC simulations. The reduced partition function ratio for Nd sorbed on ferrihydrite was then calculated by using the isotope fractionation between the experimental solution and Nd on ferrihydrite determined by the adsorption experiments ($10^3 \ln\alpha_{Sol\text{-}Liq} = -0.113$; Table 5). This results in a hypothetical isotope fractionation between seawater and ferrihydrite of 0.215 ‰ which is significantly larger than the isotope fractionation observed in the adsorption experiments alone (0.113 ‰) and is closer to the difference in isotopic composition between Nd in natural seawater and Fe-Mn (hydr)oxides of 0.357 ‰ (Fig. 7).

Table 5. $10^3 \ln\beta$ values of Nd in aqueous solutions, simplified seawater, and sorbed to ferrihydrite.

Species	$10^3 \ln\beta$ (25 °C)
Seawater	0.997
Experiment solution	0.898
Ferrihydrite (surface complex)	0.785

Previous adsorption experiments have also shown that the fractionation between REE in aqueous solution and birnessite follow the same direction as for ferrihydrite observed here, with an even larger magnitude of isotope fractionation ($\Delta^{146}Nd_{Sol\text{-}Liq}$ = 0.410 ‰ for Nd on birnessite versus 0.166 ‰ for Nd on ferrihydrite; Nakada et al., 2013a,b). The larger isotope fractionation on Mn-oxides can explain the remaining offset between Fe-Mn-oxides in marine sediments and adsorption experiments.

In addition, these two sample sets are from vastly different locations (Seaham, northeast coast of England and Pigafetta Basin, western Pacific) and marine environments

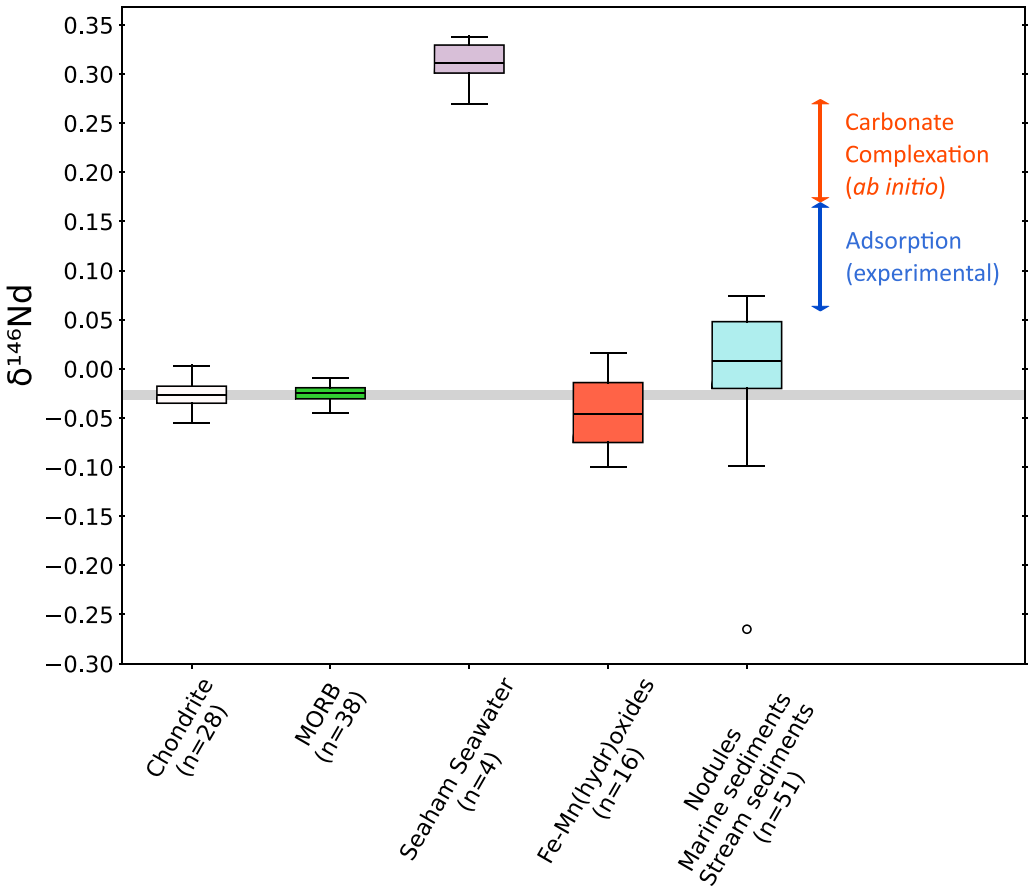

Figure 7. The Isotopic composition of Fe-Mn(hydr)oxides from a marine sediment core (Bai et al., 2025) and seawater samples (this study) is compared with experimental fractionations. Chondrite and mid-ocean ridge basalt (MORB) are shown for reference as they closely resemble bulk silicate Earth (McCoy-West et al., 2021, 2017). The grey bar represents chondritic composition (-0.027 ± 0.005 ‰). Experimental predictions of the isotope fractionation (blue arrow) and carbonate complexation (orange arrow) agree with observations in natural samples. Data of nodules, marine sediments, and stream sediments are from Bai et al. (2021), Bai et al. (2022), Bai et al. (2025) Liu et al. (2023), Ma et al. (2013), and Yu et al. (2025).

(coastal versus deep marine, respectively). Isotopic heterogeneities for $^{143}Nd/^{144}Nd$ in the ocean are well known (Lacan et al., 2012; Piepgras and Wasserburg, 1980; van de Flierdt et al., 2016) while this study presents the first stable $\delta^{146}Nd$ data. The short residence time of Nd can cause isotopic heterogeneities in the ocean and it has been shown that deep marine environments are greatly influenced by benthic trace element fluxes compared to coastal waters (Du et al., 2025; Haley et al., 2017). In addition, Nd adsorbs in shallow waters onto scavenger minerals (e.g. Fe and Mn oxides) and can desorb again in deep waters (Sholkovitz et al., 1994) while further mineral dissolution and precipitation processes may affect the bonding of Nd between shallow to deep marine settings (Basak et al., 2024). Overall, potential heterogeneities in the composition of global seawater and ferromanganese crust are not quantified to date but could be substantial, thereby explaining the large discrepancy between the experimental and natural isotope fractionation. A larger dataset of natural samples is warranted to elucidate the isotope fractionation between sinks and sources in the ocean.

In summary, heavy Nd isotopes in natural waters can be explained by an interplay of (1) scavenging of lighter Nd isotopes by Fe-Mn (hydr)oxides and (2) the high proportion of carbonate species of Nd in seawater which increases the magnitude of isotope fractionation.

4.3 Effects of metal complexation on isotope fractionation

No variation in isotope fractionation was found for Ce on ferrihydrite with increasing pH and hence the proportion of carbonate complexes (Nakada et al., 2017). This suggests that carbonate speciation and, therefore, solution speciation has no effect on isotope fractionation of REE in aqueous solution and on ferrihydrite. However, ab initio calculations by Nakada et al. (2017) found that a bidentate $CeCO_3(H_2O)_7^+$ is depleted in $^{142}Ce/^{140}Ce$ compared to $Ce(H_2O)_9^{3+}$ by only 0.038 ‰. Similarly, Nestmeyer and McCoy-West (2025) found an even more limited fractionation of 0.010 ‰ between $Ce(H_2O)_9^{3+}$ and monodentate $CeCO_3(H_2O)_8^+$ with the carbonate complex also being lighter. This is also consistent with theoretical predictions by Schauble (2024) who found indistinguishable isotope fractionation between $CeCO_3(H_2O)_7^+$ and $Ce(H_2O)_9^{3+}$

with both having a β-factor of 1.03 ‰ at 25 °C. Likewise, Liu et al. (2025a) found monodentate $CeCO_3(H_2O)_8^+$ enriched in $^{136}Ce/^{142}Ce$ by 0.01 ‰ compared to $Ce(H_2O)_9^{3+}$. These theoretical predictions all point toward very limited fractionation between free Ce^{3+} and $CeCO_3^+$ complexes. In contrast, theoretical fractionation between $Nd(H_2O)_9^{3+}$ and a monodentate $NdCO_3(H_2O)_7^+$ is significant at 0.107 ‰ at 25 °C with the carbonate complex being isotopically heavier (Nestmeyer and McCoy-West, 2025). Collectively, these observations should result in a much larger fractionation between Nd in seawater and Nd on ferrihydrite than observed in experiments compared to Ce. Notably, a pH dependent isotope fractionation between Ce in aqueous solution and Ce on birnessite was observed by Nakada et al. (2017). A pH dependent isotope fractionation was also found for Ca and Zn on birnessite and has been attributed to a change in surface complexation from interlayer vacancies only to interlayer plus edge sites (Schmitt et al., 2024; Wang et al., 2023). A pH-dependent effect on the isotope fractionation of Ce on birnessite is best explained by a change in surface complexation with changing pH rather than a change in the proportion of aqueous $CeCO_3^+$ complexes. A significantly different effect of the presence of carbonate complexes on the isotope fractionation is therefore possible for Nd.

Another issue is that most metals like Ni, Cu, and Zn are strongly complexed by dissolved organics in seawater (Moffett and Boiteau, 2024). Unfortunately, databases for thermodynamic speciation modelling like the one used here do not contain data for organic complexes of REE and furthermore the nature of the organic REE complexes remains unknown. The significance of the organic speciation of REE in seawater is poorly understood and cannot be assessed here. Ab initio calculations of metals bound to organic complexes have shown that organic complexes are usually isotopically heavier than free hydrated metals (Fujii et al., 2014; Mahan et al., 2024; Sherman, 2013) similar to the carbonate complex. The organic complexation of Nd in seawater might, therefore, not substantially modify the isotope fractionation between seawater and ferrihydrite predicted here, and could in fact amplify the fractionation, although this remains an open question.

4.4 Comparison with previous adsorption experiments

Previous adsorption experiments of Ce on ferrihydrite by Nakada et al. (2013a) found enrichment of light Ce in the solid phase similar to the finding in this study. They found an isotope fractionation of $\Delta^{142/140}Ce_{Liquid\text{-}Solid}$ of 0.145 ‰ which is similar to the fractionation found in this study ($\Delta^{146/144}Nd_{Liquid\text{-}Solid} = 0.113$ ‰). The $^{142}Ce/^{140}Ce$ ratio has a relative mass difference $(m_1 - m_2)/((m_1 + m_2)/2)$ of 0.0142 which is very similar to the $^{146}Nd/^{144}Nd$ ratio which has a relative mass difference of 0.0138. Therefore, a similar magnitude of isotope fractionation would be expected.

For the adsorption of Nd and Sm on ferrihydrite, Nakada et al. (2013b) found an isotope fractionation between aqueous and surface complex of $^{145}Nd/^{143}Nd = -0.166$ ‰ and $^{149}Sm/^{147}Sm = -0.206$ ‰ with the solid phase enriched in heavier isotopes. This is in stark contrast to the isotope fractionation observed here. Although a different isotope pair of Nd ($^{145}Nd/^{143}Nd$) was used by Nakada et al. (2013b), the results should be directly comparable because of the very similar relative mass difference of 0.0139.

Several factors are discussed below which could explain why the direction of isotope fractionation might be different in the experiments by Nakada et al. (2013b): 1) isotopic equilibrium in the experiments, 2) formation of different surface complexes, 3) speciation of Nd in the aqueous solution, 4) using freeze dried versus freshly prepared ferrihydrite or 5) loss of Nd during ion-exchange chromatography:

1) A major consideration is isotopic equilibrium in the absorption experiments. The time required to achieve isotopic equilibrium has been shown here to be ≥ 24 h which is longer than the duration of 6 h used in the adsorption experiments by Nakada et al. (2013b). However, as shown herein, the solid phase was preferentially enriched in lighter isotopes when kinetic isotope effects dominated, but at no point was the solid phase enriched in heavier isotopes (Fig. 2a). Therefore, although disequilibrium may play a role, it probably cannot explain the large discrepancy observed.
2) Large discrepancies in fractionation have been observed when the coordination of surface complexes is considerably different (e.g. Zn forms octahedral or tetrahedral complexes; Wang et al., 2023). As mentioned above, differences in surface complexation driven by pH have been found on birnessite. However, adsorption experiments of Ce on ferrihydrite conducted at variable pH (6.8–11.0) did not show pH dependent isotope fractionation during adsorption (Nakada et al., 2017). It would be expected all REE exhibit similar behaviour.
3) Solution chemistry and metal speciation has been shown to play a role in isotope fractionation but is not significant enough to explain this discrepancy (Dong and Wasylenki, 2016; Jiskra et al., 2012). A 0.1 M NaCl background solution and pH of 5.0 was used by Nakada et al. (2013b). This is similar to the pH and background electrolyte concentration used in this study which should result in the formation of a small proportion of Cl^- complexes which unlikely causes such a different outcome. According to thermodynamic modelling, the majority of Nd will still be present as a free Nd^{3+} complex (96 %) is also the dominant species in the experiments by Nakada et al. (2013b) as demonstrated by speciation modelling therein.
4) Another potential cause is the freeze drying of ferrihydrite. Nakada et al. (2013b) introduced freeze dried ferrihydrite to their experiments which has been demonstrated to modify the morphology of ferrihydrite (Greffié et al., 2001) which could have caused a different coordination of Nd. However, this effect is likely also limited, for example, Ijichi et al. (2018) compared freeze dried and freshly prepared birnessite in adsorption experiments with Cu and this did not significantly change the outcome of the adsorption experiments.

5) Nakada reports a recovery of > 99 % but did not use a double spike which also corrects for isotope fractionation occurring during sample preparation. Potentially, isotope fractionation of Nd during the sample preparation could explain the opposing outcome in Nakada et al. (2013b). Significant isotope fractionation of Nd during ion-exchange chromatography up to 0.448 ‰ was reported by Liu et al. (2023). However, given the excellent yields quoted this effect would be insignificant.

The reason why previous adsorption experiments observed enrichment of heavy Nd on ferrihydrite remains enigmatic. Enrichment of lighter Nd on birnessite has also been observed recently using a double spike (Stewart et al., 2024), which is also the opposite of what has been found by Nakada et al. (2013b). Adsorption experiments with Ce on ferrihydrite (Nakada et al., 2013a) agree with the results presented here. Furthermore, the results presented in this study agree with observations and magnitude of isotope fractionation observed in natural samples. Given that Ce and Nd are isotopically lighter on ferrihydrite, enrichment of lighter isotopes on Fe-Mn (hydr)oxides is presumably the case for all the light REE.

5 Conclusions

The isotope fractionation between Nd in aqueous solution and ferrihydrite observed herein is opposite to what has previously been reported. Isotopic equilibrium is achieved after $\geq$ 24 h and Nd on ferrihydrite is enriched in lighter isotopes by 0.113 ‰ relative to Nd in aqueous solution. This observation agrees with previous experiments on Ce isotope fractionation on ferrihydrite. In agreement with previous EXAFS analyses, MD simulations demonstrate that, in equilibrium, Nd forms a bidentate inner-sphere surface complex on ferrihydrite. Enrichment of lighter isotopes in the surface complex is best explained by the stiffer bonds in the aqueous complex. In seawater, the speciation of Nd is vastly different compared to the synthetic solutions used in the adsorption experiments. The predominance of carbonate complexes of Nd can be expected to increase the isotope fractionation in nature to 0.215 ‰. This does not perfectly agree with the, so far, limited data of natural seawaters and Fe-Mn (hydr)oxides from marine sediments. The scavenging of lighter Nd isotopes on ferromanganese crusts is proposed to form a large sink of lighter Nd isotopes in the ocean which leaves seawater enriched in heaver Nd isotopes. This enhances our understanding of the geochemical cycle of Nd and is also applicable to other light REE.

Acknowledgements

We thank Brendan Jones for his help with performing the XRD analysis. We are thankful to Dave Sherman for his help with the molecular dynamic simulations. The ab initio molecular dynamics simulations were supported by high performance computer resources at Pawsey Supercomputer Centre with funding from the Australian Government and the Government of Western Australia. We thank Huiqing Huang, Anne Kaufmann, and Sminto Augustine for assistance with the clean laboratory work and instrumental analyses at JCU. Josh Grattage is thanked for help with processing seawater samples. Geoff Nowell is thanked for impeccable maintenance of the TIMS instrument at Durham. This project was supported by ARC grant DE210101395 to AMW and NERC grant NE/N003926/1 to KWB. We thank Jianghao Bai, Andrew Frierdich, Maxwell Lechte, and one anonymous reviewer for comments that improved the quality of the manuscript. Ryan Ickert, Daniel Ibarra, and Claire Rollion-Bard are thanked for comments and the editorial handling.

Data, code, and outputs availability

Data are available through Research Data JCU at https://doi.org/10.25903/tfqa-tt39 (Nestmeyer et al., 2026). The Supplementary Material includes 3 figures and 2 tables. Main text figures and tables are available for download in the online version of this article.

Competing interests

The authors declare no competing interests.

Licence agreement

References

Allen PG, Bucher JJ, Shuh DK, Edelstein NM, Craig I (2000). Coordination chemistry of trivalent lanthanide and actinide ions in dilute and concentrated chloride solutions. *Inorganic Chemistry* 39(3): 595–601. doi:10.1021/ic9905953

Bai J, Deng Y, Wu H, Liang X, Yu X, Zhang G, Wei G (2025). Stable Nd isotopic fractionation in REY-rich deep-sea sediments. *Earth and Planetary Science Letters* 652: 119197. doi:10.1016/j.epsl.2024.119197

Bai J, Liu F, Zhang ZF, Ma JL, Zhang L, Liu YF, Zhong SX, Wei GJ (2021). Simultaneous measurement stable and radiogenic Nd isotopic compositions by MC-ICP-MS with a single-step chromatographic extraction technique. *Journal of Analytical Atomic Spectrometry* 36(12): 2695–2703. doi:10.1039/d1ja00302j

Bai J, Luo K, Wu C, Wang Z, Zhang L, Yan S, Zhong S, Ma J, Wei G (2023). Stable neodymium isotopic fractionation during chemical weathering. *Earth and Planetary Science Letters* 617: 118260. doi:10.1016/j.epsl.2023.118260

Bai J, Ma J, Wei G, Zhang L, Liu C, Gao T, Liu Y, Liu Y (2022). Stable neodymium isotope ratios of geological reference materials. *Geostandards and Geoanalytical Research* 46(4): 825–836. doi:10.1111/ggr.12451

Bai J, Wu C, Wu H, Wang Z, Zhang L, Zhong S, Ma J, Wei G (2024). δ^{142}Ce minus δ^{146}Nd value as a redox indicator in Earth's surface environments. *Earth and Planetary Science Letters* 629: 118597. doi:10.1016/j.epsl.2024.118597

Balistrieri LS, Borrok DM, Wanty RB, Ridley WI (2008). Fractionation of Cu and Zn isotopes during adsorption onto amorphous Fe(III) oxyhydroxide: Experimental mixing of acid rock drainage and ambient river water. *Geochimica et Cosmochimica Acta* 72(2): 311–328. doi:10.1016/j.gca.2007.11.013

Barling J, Anbar AD (2004). Molybdenum isotope fractionation during adsorption by manganese oxides. *Earth and Planetary Science Letters* 217(3-4): 315–329. doi:10.1016/S0012-821X(03)00608-3

Basak C, Wu Y, Haley BA, Muratli J, Pena LD, Bolge L, Fitzsimmons JN, Sherrell RM, Goldstein SL (2024). Suspended particulate matter influence on dissolved Nd concentration and isotopic composition along GEOTRACES section GP16. *Earth and Planetary Science Letters* 635: 118692. doi:10.1016/j.epsl.2024.118692

Bau M (1999). Scavenging of dissolved yttrium and rare earths by precipitating iron oxyhydroxide: experimental evidence for Ce oxidation, Y-Ho fractionation, and lanthanide tetrad effect. *Geochimica et Cosmochimica Acta* 63(1): 67–77. doi:10.1016/S0016-7037(99)00014-9

Bigeleisen J, Mayer MG (1947). Calculation of Equilibrium Constants for Isotopic Exchange Reactions. *The Journal of Chemical Physics* 15(5): 261–267. doi:10.1063/1.1746492

Brennecka GA, Wasylenki LE, Bargar JR, Weyer S, Anbar AD (2011). Uranium isotope fractionation during adsorption to Mn-oxyhydroxides. *Environmental Science & Technology* 45(4): 1370–5. doi:10.1021/es103061v

Brugger J, Liu W, Etschmann B, Mei Y, Sherman DM, Testemale D (2016). A review of the coordination chemistry of hydrothermal systems, or do coordination changes make ore deposits? *Chemical Geology* 447: 219–253. doi:10.1016/j.chemgeo.2016.10.021

Campbell L, Rehr J, Schenter G, McCarthy M, Dixon D (1999). XAFS Debye–Waller factors in aqueous Cr+3 from molecular dynamics. *Synchrotron Radiation* 6(3): 310–312. doi:10.1107/S0909049598018202

Cornell RM, Schwertmann U (2003). *The iron oxides: structure, properties, reactions, occurrences and uses*. Wiley-VCH, Weinheim, 2nd edn. doi:10.1002/3527602097

De Baar H, Schijf J, Byrne R (1991). Solution chemistry of the rare earth elements in seawater. *European Journal of Solid State and Inorganic Chemistry* 28: 357–373

Diehl A, Bach W (2020). MARHYS (MARine HYdrothermal Solutions) Database: A Global Compilation of Marine Hydrothermal Vent Fluid, End Member, and Seawater Compositions. *Geochemistry, Geophysics, Geosystems* 21(12). doi:10.1029/2020gc009385

Dodson M (1963). A theoretical study of the use of internal standards for precise isotopic analysis by the surface ionization technique: Part I-General first-order algebraic solutions. *Journal of Scientific Instruments* 40(6): 289. doi:10.1088/0950-7671/40/6/307

Dong S, Wasylenki LE (2016). Zinc isotope fractionation during adsorption to calcite at high and low ionic strength. *Chemical Geology* 447: 70–78. doi:10.1016/j.chemgeo.2016.10.031

Drits V, Sakharov B, Salyn A, Manceau A (1993). Structural model for ferrihydrite. *Clay Minerals* 28(2): 185–207. doi:10.1180/claymin.1993.028.2.02

Du J, Haley BA, McManus J, Blaser P, Rickli J, Vance D (2025). Abyssal seafloor as a key driver of ocean trace-metal biogeochemical cycles. *Nature* 642(8068): 620–627. doi:10.1038/s41586-025-09038-3

van de Flierdt T, Griffiths AM, Lambelet M, Little SH, Stichel T, Wilson DJ (2016). Neodymium in the oceans: a global database, a regional comparison and implications for palaeoceanographic research. *Philosophical Transactions of the Royal Society A: Mathematical, Physical and Engineering Sciences* 374(2081): 20150293. doi:10.1098/rsta.2015.0293

Fujii T, Moynier F, Blichert-Toft J, Albarède F (2014). Density functional theory estimation of isotope fractionation of Fe, Ni, Cu, and Zn among species relevant to geochemical and biological environments. *Geochimica et Cosmochimica Acta* 140: 553–576. doi:10.1016/j.gca.2014.05.051

Goldberg T, Archer C, Vance D, Poulton SW (2009). Mo isotope fractionation during adsorption to Fe (oxyhydr)oxides. *Geochimica et Cosmochimica Acta* 73(21): 6502–6516. doi:10.1016/j.gca.2009.08.004

Greffié C, Amouric M, Parron C (2001). HRTEM study of freeze-dried and untreated synthetic ferrihydrites: consequences of sample processing. *Clay Minerals* 36(3): 381–387. doi:10.1180/000985501750539472

Grimme S, Antony J, Ehrlich S, Krieg H (2010). A consistent and accurate ab initio parametrization of density functional dispersion correction (DFT-D) for the 94 elements H-Pu. *The Journal of Chemical Physics* 132(15): 154104. doi:10.1063/1.3382344

Guan Q, Mei Y, Etschmann B, Testemale D, Louvel M, Brugger J (2020). Yttrium complexation and hydration in chloride-rich hydrothermal fluids: A combined ab initio molecular dynamics and in situ X-ray absorption spectroscopy study. *Geochimica et Cosmochimica Acta* 281: 168–189. doi:10.1016/j.gca.2020.04.015

Habenschuss A, Spedding FH (1979). The coordination (hydration) of rare earth ions in aqueous chloride solutions from x-ray diffraction. II. $LaCl_3$, $PrCl_3$, and $NdCl_3$. *The Journal of Chemical Physics* 70(8): 3758–3763. doi:10.1063/1.437928

Haley BA, Du J, Abbott AN, McManus J (2017). The impact of benthic processes on rare earth element and neodymium isotope distributions in the oceans. *Frontiers in Marine Science* 4: 426. doi:10.3389/fmars.2017.00426

Hamilton P, O'Nions R, Bridgwater D, Nutman A (1983). Sm-Nd studies of Archaean metasediments and metavolcanics from West Greenland and their implications for the Earth's early history. *Earth and Planetary Science Letters* 62(2): 263–272. doi:10.1016/0012-821X(83)90089-4

Hiemstra T (2013). Surface and mineral structure of ferrihydrite. *Geochimica et Cosmochimica Acta* 105: 316–325. doi:10.1016/j.gca.2012.12.002

Hiemstra T, Antelo J, Rahnemaie R, van Riemsdijk WH (2010). Nanoparticles in natural systems I: The effective reactive surface area of the natural oxide fraction in field samples. *Geochimica et Cosmochimica Acta* 74(1): 41–58. doi:10.1016/j.gca.2009.10.018

Huang F, Zhou C, Wang W, Kang J, Wu Z (2019). First-principles calculations of equilibrium Ca isotope fractionation: Implications for oldhamite formation and evolution of lunar magma ocean. *Earth and Planetary Science Letters* 510: 153–160. doi:10.1016/j.epsl.2018.12.034

Humphrey W, Dalke A, Schulten K (1996). VMD: visual molecular dynamics. *Journal of Molecular Graphics* 14(1): 33–38. doi:10.1016/0263-7855(96)00018-5

Ijichi Y, Ohno T, Sakata S (2018). Copper isotopic fractionation during adsorption on manganese oxide: Effects of pH and desorption. *Geochemical Journal* 52(2): e1–e6. doi:10.2343/geochemj.2.0516

Ishiguro S, Umebayashi Y, Komiya M (2002). Thermodynamic and structural aspects on the solvation steric effect of lanthanide(III)—dependence on the ionic size. *Coordination Chemistry Reviews* 226(1-2): 103–111. doi:10.1016/s0010-8545(01)00448-9

Jacobsen SB, Wasserburg G (1980). Sm-Nd isotopic evolution of chondrites. *Earth and Planetary Science Letters* 50(1): 139–155. doi:10.1016/0012-821X(80)90125-9

Jiskra M, Wiederhold JG, Bourdon B, Kretzschmar R (2012). Solution speciation controls mercury isotope fractionation of Hg (II) sorption to goethite. *Environmental Science & Technology* 46(12): 6654–6662. doi:10.1021/es3008112

Juillot F, Maréchal C, Ponthieu M, Cacaly S, Morin G, Benedetti M, Hazemann JL, Proux O, Guyot F (2008). Zn isotopic fractionation caused by sorption on goethite and 2-Lines ferrihydrite. *Geochimica et Cosmochimica Acta* 72(19): 4886–4900. doi:10.1016/j.gca.2008.07.007

Kaufmann AK, McCoy-West AJ (2025). Combined Stable and Radiogenic Nd Isotope Characterisation of Sedimentary and Iron Formation Reference Materials by Double Spike MC-ICP-MS. *Geostandards and Geoanalytical Research* 50(1): 221–240. doi:10.1111/ggr.70020

Kühne TD, Iannuzzi M, Del Ben M, Rybkin VV, Seewald P, Stein F, Laino T, Khaliullin RZ, Schütt O, Schiffmann F, et al. (2020). CP2K: An electronic structure and molecular dynamics software package-Quickstep: Efficient and accurate electronic structure calculations. *The Journal of Chemical Physics* 152(19). doi:10.1063/5.0007045

Lacan F, Tachikawa K, Jeandel C (2012). Neodymium isotopic composition of the oceans: A compilation of seawater data. *Chemical Geology* 300: 177–184. doi:10.1016/j.chemgeo.2012.01.019

Li W, Liu XM, Nakada R, Takahashi Y, Hu Y, Shakouri M, Zhang Z, Okumura T, Yamada S (2023). The cerium isotope fingerprints of redox fluctuation in bauxites. *Earth and Planetary Science Letters* 602: 117962. doi:10.1016/j.epsl.2022.117962

Li W, Nakada R, McManus J, Haley BA, Shakouri M, Li F, Takahashi Y (2025). Decoupling cerium isotope fractionation from cerium anomalies in marine sediments. *Earth and Planetary Science Letters* 671: 119652. doi:10.1016/j.epsl.2025.119652

Little SH, Sherman DM, Vance D, Hein J (2014). Molecular controls on Cu and Zn isotopic fractionation in Fe–Mn crusts. *Earth and Planetary Science Letters* 396: 213–222. doi:10.1016/j.epsl.2014.04.021

Liu B, Zhu G, Ma J, Zhang L, Wei G (2024). Equilibrium fractionation of stable strontium isotopes during adsorption to Mn oxides. *Geochemistry, Geophysics, Geosystems* 25(4): e2024GC011460. doi:10.1029/2024GC011460

Liu F, Li X, Yang H, Peng Q, Wu J, Zhang Z (2023). Simultaneously obtaining stable and radiogenic Nd isotope ratios through a single DGA column using double spike TIMS. *Journal of Analytical Atomic Spectrometry* 38(12): 2581–2589. doi:10.1039/d3ja00284e

Liu F, Zhang Y, Liu Y, Zhang Z, Li X (2025a). Stable cerium isotopes as a potential new redox proxy: Insight from first-principles calculations. *Chemical Geology* 690: 122856. doi:10.1016/j.chemgeo.2025.122856

Liu F, Zhu H, Perfit MR, Li X, An Y, Ling M, Zhang Z (2025b). Cerium isotopic fractionation during magmatic processes and the composition of the upper mantle. *Earth and Planetary Science Letters* 661: 119365. doi:10.1016/j.epsl.2025.119365

Ma J, Wei G, Liu Y, Ren Z, Xu Y, Yang Y (2013). Precise measurement of stable neodymium isotopes of geological materials by using MC-ICP-MS. *Journal of Analytical Atomic Spectrometry* 28(12): 1926–1931. doi:10.1039/c3ja50229e

Mahan B, Hu Y, Lahoud E, Nestmeyer M, McCoy-West A, Manestar G, Fowler C, Bush AI, Moynier F (2024). Stable potassium isotope ratios in human blood serum towards biomarker development in Alzheimer's disease. *Metallomics* 16(9): mfae038. doi:10.1093/mtomcs/mfae038

Mayanovic RA, Anderson AJ, Bassett WA, Chou IM (2009). The structure and stability of aqueous rare-earth elements in hydrothermal fluids: New results on neodymium(III) aqua and chloroaqua complexes in aqueous solutions to 500 °C and 520 MPa. *Chemical Geology* 259(1-2): 30–38. doi:10.1016/j.chemgeo.2008.08.011

McCoy-West AJ, Burton KW, Millet MA, Cawood PA (2021). The chondritic neodymium stable isotope composition of the Earth inferred from mid-ocean ridge, ocean island and arc basalts. *Geochimica et Cosmochimica Acta* 293: 575–597. doi:10.1016/j.gca.2020.09.038

McCoy-West AJ, Millet MA, Burton KW (2017). The neodymium stable isotope composition of the silicate Earth and chondrites. *Earth and Planetary Science Letters* 480: 121–132. doi:10.1016/j.epsl.2017.10.004

McCoy-West AJ, Millet MA, Burton KW (2020a). The Neodymium Stable Isotope Composition of the Oceanic Crust: Reconciling the Mismatch Between Erupted Mid-Ocean Ridge Basalts and Lower Crustal Gabbros. *Frontiers in Earth Science* 8. doi:10.3389/feart.2020.00025

McCoy-West AJ, Millet MA, Nowell GM, Nebel O, Burton KW (2020b). Simultaneous measurement of neodymium stable and radiogenic isotopes from a single aliquot using a double spike. *Journal of Analytical Atomic Spectrometry* 35(2): 388–402. doi:10.1039/c9ja00308h

McCoy-West AJ, Mortimer N, Burton KW, Ireland TR, Cawood PA (2022). Re-initiation of plutonism at the Gondwana margin after a magmatic hiatus: The bimodal Permian-Triassic Longwood Suite, New Zealand. *Gondwana Research* 105: 432–449. doi:10.1016/j.gr.2021.09.021

Mei Y, Liu W, Brugger J, Guan Q (2020). Gold solubility in alkaline and ammonia-rich hydrothermal fluids: Insights from ab initio molecular dynamics simulations. *Geochimica et Cosmochimica Acta* 291: 62–78. doi:10.1016/j.gca.2019.12.031

Michel FM, Ehm L, Antao SM, Lee PL, Chupas PJ, Liu G, Strongin DR, Schoonen MA, Phillips BL, Parise JB (2007). The structure of ferrihydrite, a nanocrystalline material. *Science* 316(5832): 1726–9. doi:10.1126/science.1142525

Moffett JW, Boiteau RM (2024). Metal organic complexation in seawater: Historical background and future directions. *Annual Review of Marine Science* 16(1): 577–599. doi:10.1146/annurev-marine-033023-083652

Momma K, Izumi F (2011). VESTA 3 for three-dimensional visualization of crystal, volumetric and morphology data. *Applied Crystallography* 44(6): 1272–1276. doi:10.1107/S0021889811038970

Nakada R, Takahashi Y, Tanimizu M (2013a). Isotopic and speciation study on cerium during its solid–water distribution with implication for Ce stable isotope as a paleo-redox proxy. *Geochimica et Cosmochimica Acta* 103: 49–62. doi:10.1016/j.gca.2012.10.045

Nakada R, Tanaka M, Tanimizu M, Takahashi Y (2017). Aqueous speciation is likely to control the stable isotopic fractionation of cerium at varying pH. *Geochimica et Cosmochimica Acta* 218: 273–290. doi:10.1016/j.gca.2017.09.019

Nakada R, Tanimizu M, Takahashi Y (2013b). Difference in the stable isotopic fractionations of Ce, Nd, and Sm during adsorption on iron and manganese oxides and its interpretation based on their local structures. *Geochimica et Cosmochimica Acta* 121: 105–119. doi:10.1016/j.gca.2013.07.014

Narten AH, Hahn RL (2002). Hydration of the neodymium(3+) ion in neodymium chloride solutions determined by neutron diffraction. *The Journal of Physical Chemistry* 87(17): 3193–3197. doi:10.1021/j100240a007

Nestmeyer M, McCoy-West AJ (2025). Quantifying mass-dependent isotope fractionation and nuclear field shift effects for the light rare Earth elements in hydrous systems. *Geochimica et Cosmochimica Acta* 388: 236–252. doi:10.1016/j.gca.2024.10.007

Nestmeyer M, McCoy-West AJ (2026). Neodymium stable isotope fractionation in minerals: Implications for Earth's differentiation, and planetary formation. *Geochimica et Cosmochimica Acta* doi:10.1016/j.gca.2026.03.022

Nestmeyer M, McCoy-West AJ, Mei Y, Burton KW (2026). Nd isotope fractionation on ferrihydrite. James Cook University. doi:10.25903/tfqa-tt39

Nielsen SG, Wasylenki LE, Rehkämper M, Peacock CL, Xue Z, Moon EM (2013). Towards an understanding of thallium isotope fractionation during adsorption to manganese oxides. *Geochimica et Cosmochimica Acta* 117: 252–265. doi:10.1016/j.gca.2013.05.004

Nosé S (1984). A unified formulation of the constant temperature molecular dynamics methods. *The Journal of Chemical Physics* 81(1): 511–519. doi:10.1063/1.447334

Pahnke K, Van de Flierdt T, Jones KM, Lambelet M, Hemming SR, Goldstein SL (2012). GEOTRACES intercalibration of neodymium isotopes and rare earth element concentrations in seawater and suspended particles. Part 2: Systematic tests and baseline profiles. *Limnology and Oceanography: Methods* 10(4): 252–269. doi:10.4319/lom.2012.10.252

Parkhurst DL, Appelo CAJ (2013). Description of input and examples for PHREEQC version 3: a computer program for speciation, batch-reaction, one-dimensional transport, and inverse geochemical calculations. *US Geological Survey Techniques and Methods* 6-A43: 497 p. doi:10.3133/tm6A43

Perdew JP, Burke K, Ernzerhof M (1996). Generalized gradient approximation made simple. *Physical Review Letters* 77(18): 3865–3868. doi:10.1103/PhysRevLett.77.3865

Persson I, D'Angelo P, De Panfilis S, Sandstrom M, Eriksson L (2008). Hydration of lanthanoid(III) ions in aqueous solution and crystalline hydrates studied by EXAFS spectroscopy and crystallography: the myth of the "gadolinium break". *Chemistry* 14(10): 3056–66. doi:10.1002/chem.200701281

Piepgras DJ, Wasserburg G (1980). Neodymium isotopic variations in seawater. *Earth and Planetary Science Letters* 50(1): 128–138. doi:10.1016/0012-821X(80)90124-7

Pinney N, Kubicki JD, Middlemiss DS, Grey CP, Morgan D (2009). Density Functional Theory Study of Ferrihydrite and Related Fe-Oxyhydroxides. *Chemistry of Materials* 21(24): 5727–5742. doi:10.1021/cm9023875

Pourkhorsandi H, Debaille V, de Jong J, Armytage RMG (2021). Cerium stable isotope analysis of synthetic and terrestrial rock reference materials by MC-ICPMS. *Talanta* 224: 121877. doi:10.1016/j.talanta.2020.121877

Schauble EA (2004). Applying Stable Isotope Fractionation Theory to New Systems. *Reviews in Mineralogy and Geochemistry* 55(1): 65–111. doi:10.2138/gsrmg.55.1.65

Schauble EA (2011). First-principles estimates of equilibrium magnesium isotope fractionation in silicate, oxide, carbonate and hexaaquamagnesium(2+) crystals. *Geochimica et Cosmochimica Acta* 75(3): 844–869. doi:10.1016/j.gca.2010.09.044

Schauble EA (2023). Nuclear volume isotope fractionation of europium and other lanthanide elements. *Geochemical Journal* 57(4): 118–133. doi:10.2343/geochemj.GJ23010

Schauble EA (2024). Nuclear volume and mass dependent fractionation of cerium isotopes. *Geochemical Journal* 58(6): 227–245. doi:10.2343/geochemj.GJ24019

Schmitt AD, Gangloff S, Brazier JM, Nuvoli N, Tertre E (2024). Corrigendum to" Calcium isotope fractionation associated with adsorption and desorption on/from δ-MnO 2"[Geochim. Cosmochim. Acta 354 (2023) 109–122]. *Geochimica et Cosmochimica Acta* 379: 244–244. doi:10.1016/j.gca.2024.05.016

Sherman DM (2013). Equilibrium isotopic fractionation of copper during oxidation/reduction, aqueous complexation and ore-forming processes: Predictions from hybrid density functional theory. *Geochimica et Cosmochimica Acta* 118: 85–97. doi:10.1016/j.gca.2013.04.030

Sherman DM, Little SH (2020). Isotopic disequilibrium of Cu in marine ferromanganese crusts: Evidence from ab initio predictions of Cu isotope fractionation on sorption to birnessite. *Earth and Planetary Science Letters* 549: 116540. doi:10.1016/j.epsl.2020.116540

Shiery RC, Fulton JL, Balasubramanian M, Nguyen MT, Lu JB, Li J, Rousseau R, Glezakou VA, Cantu DC (2021). Coordination sphere of lanthanide aqua ions resolved with ab initio molecular dynamics and X-ray absorption spectroscopy. *Inorganic Chemistry* 60(5): 3117–3130. doi:10.1021/acs.inorgchem.0c03438

Sholkovitz ER, Landing WM, Lewis BL (1994). Ocean particle chemistry: the fractionation of rare earth elements between suspended particles and seawater. *Geochimica et Cosmochimica Acta* 58(6): 1567–1579. doi:10.1016/0016-7037(94)90559-2

Solera JA, Garcia J, Proietti MG (1995). Multielectron excitations at the L edges in rare-earth ionic aqueous solutions. *Physical Review B* 51(5): 2678–2686. doi:10.1103/physrevb.51.2678

Spadini L, Schindler PW, Charlet L, Manceau A, Ragnarsdottir KV (2003). Hydrous ferric oxide: evaluation of Cd–HFO surface complexation models combining CdK EXAFS data, potentiometric titration results, and surface site structures identified from mineralogical knowledge. *Journal of Colloid and Interface Science* 266(1): 1–18. doi:10.1016/S0021-9797(03)00504-6

Steele ML, Wertz DL (1977). Solvent effects on the coordination of neodymium(3+) ions in concentrated neodymium trichloride solutions. *Inorganic Chemistry* 16(5): 1225–1228. doi:10.1021/ic50171a050

Stewart BW, Capo RC, Schaffer CR, Stuckman M, Lopano CL (2024). Understanding REE accumulation in acid mine drainage treatment precipitates through isotopic fractionation of neodymium during adsorption on hydrous manganese oxides. *2024 Goldschmidt Conference* doi:10.46427/gold2024.24689

Turner D, Whitfield M, Dickson A (1981). The equilibrium speciation of dissolved components in freshwater and sea water at 25 °C and 1 atm pressure. *Geochimica et Cosmochimica Acta* 45(6): 855–881. doi:10.1016/0016-7037(81)90115-0

Urey HC (1947). The thermodynamic properties of isotopic substances. *Journal of the Chemical Society* pp. 562–581. doi:10.1039/jr9470000562

VandeVondele J, Hutter J (2007). Gaussian basis sets for accurate calculations on molecular systems in gas and condensed phases. *The Journal of Chemical Physics* 127(11). doi:10.1063/1.2770708

VandeVondele J, Krack M, Mohamed F, Parrinello M, Chassaing T, Hutter J (2005). Quickstep: Fast and accurate density functional calculations using a mixed Gaussian and plane waves approach. *Computer Physics Communications* 167(2): 103–128. doi:10.1016/j.cpc.2004.12.014

Wang Z, Peacock C, Kwon KD, Gu X, Feng X, Li W (2023). Site-specific isotope fractionation during Zn adsorption onto birnessite: Insights from X-ray absorption spectroscopy, density functional theory and surface complexation modeling. *Geochimica et Cosmochimica Acta* 348: 68–84. doi:10.1016/j.gca.2023.03.006

Wasylenki LE, Howe HD, Spivak-Birndorf LJ, Bish DL (2015). Ni isotope fractionation during sorption to ferrihydrite: Implications for Ni in banded iron formations. *Chemical Geology* 400: 56–64. doi:10.1016/j.chemgeo.2015.02.007

Wasylenki LE, Rolfe BA, Weeks CL, Spiro TG, Anbar AD (2008). Experimental investigation of the effects of temperature and ionic strength on Mo isotope fractionation during adsorption to manganese oxides. *Geochimica et Cosmochimica Acta* 72(24): 5997–6005. doi:10.1016/j.gca.2008.08.027

Waychunas GA, Kim CS, Banfield JF (2005). Nanoparticulate iron oxide minerals in soils and sediments: unique properties and contaminant scavenging mechanisms. *Journal of Nanoparticle Research* 7: 409–433. doi:10.1007/s11051-005-6931-x

Yamaguchi T, Nomura M, Wakita H, Ohtaki H (1988). An extended x-ray absorption fine structure study of aqueous rare earth perchlorate solutions in liquid and glassy states. *The Journal of Chemical Physics* 89(8): 5153–5159. doi:10.1063/1.455633

Yan X, Zhu M, Li W, Peacock CL, Ma J, Wen H, Liu F, Zhou Z, Zhu C, Yin H (2021). Cadmium Isotope Fractionation during Adsorption and Substitution with Iron (Oxyhydr)oxides. *Environmental Science & Technology* 55(17): 11601–11611. doi:10.1021/acs.est.0c06927

Yang J, Li Y, Liu S, Tian H, Chen C, Liu J, Shi Y (2015). Theoretical calculations of Cd isotope fractionation in hydrothermal fluids. *Chemical Geology* 391: 74–82. doi:10.1016/j.chemgeo.2014.10.029

Yu X, Bai J, Wei G, Lin M, Rudnick RL (2025). Stable neodymium isotopic composition of the upper continental crust through time from ancient glacial diamictites and Holocene marine sediments. *Geochimica et Cosmochimica Acta* doi:10.1016/j.gca.2025.10.026

Zhang G, Bai J, Zhao M, Wang P, Zhu Y, Cao J, Wu H, Xu R, He G, Wei G (2026). Cerium isotopic compositions of deep-sea sediments: implications for geochemical behavior of rare earth elements in the pelagic seafloor. *Geochimica et Cosmochimica Acta* 412: 186–198. doi:10.1016/j.gca.2025.11.015

Zhou W, Zhou A, Wen B, Liu P, Zhu Z, Finfrock Z, Zhou J (2022). Antimony isotope fractionation during adsorption on aluminum oxides. *Journal of Hazardous Materials* 429: 128317. doi:10.1016/j.jhazmat.2022.128317